Engineering Fracture Mechanics 282 (2023) 109171

Contents lists available at ScienceDirect

Engineering Fracture Mechanics

journal homepage: www.elsevier.com/locate/engfracmech

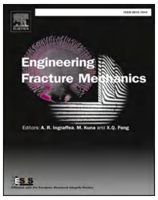

A FDEM approach to study mechanical and fracturing responses of geo-materials with high inclusion contents using a novel reconstruction strategy

Yuexiang Lin [a,b], Jianjun Ma [c,*], Zhengshou Lai [d], Linchong Huang [a,*], Mingfeng Lei [e]

[a] School of Aeronautics and Astronautics, Sun Yat-Sen University, Shenzhen 518107, China
[b] Department of Civil and Environmental Engineering, The Hong Kong Polytechnic University, Hong Kong, China
[c] School of Civil Engineering, Sun Yat-Sen University, Zhuhai 519000, China
[d] School of Intelligent Systems Engineering, Sun Yat-Sen University, Shenzhen 518107, China
[e] School of Civil Engineering, Central South University, Changsha 410075, China

ARTICLE INFO

Keywords:
Finite-discrete element method
Stochastic reconstruction
Signed-distance field-based discrete element method
Fracture analysis
Interface effects

ABSTRACT

In this paper, a detailed FDEM approach to simulate the mechanical and fracturing responses of heterogeneous geomaterials with irregular inclusions is systematically developed. The inclusion surface morphology is first obtained through 3D scanning techniques. A computational geometry method, the curvature-weighted sphere Voronoi method (CWSVM), is adopted to control the mesh quantity and quality and ensure the efficiency and accuracy of the FDEM numerical model. A signed-distance-field-based discrete element method (SDF-DEM) is employed to approximate the natural distribution and orientation of inclusions. Heterogeneous geomaterials with large inclusion contents (such as 60% and 70%) are generated effectively and efficiently through this approach. Next, to model the fracturing process, a finite discrete element method (FDEM) model is developed by integrating cohesive elements into the mesh in a fast and efficient manner. In addition, a combined constitutive model is proposed to consider the shear-hardening behaviour of the cohesive elements. The proposed numerical approach is verified through comparison with experimental results, including the shape of inclusions and mechanical responses of geomaterials. The results demonstrate that both satisfactory precision and low calculation costs can be achieved using the proposed algorithm. The consequent simulation performance is verified through comparisons of observations and numerical results with experimental results for failure patterns and mechanical behaviours. In addition, the effects of the strength of the interfaces between the inclusions and matrix on the mechanical and fracturing characteristics of inclusion-containing geomaterials are analysed quantitatively. The mechanical strength decreases rather than increases with increasing content of inclusions when the interface strength is less than the matrix strength.

---

* Corresponding authors.
E-mail addresses: linyx86@mail.sysu.edu.cn (Y. Lin), majianjun@mail.sysu.edu.cn (J. Ma), laizhengsh@mail.sysu.edu.cn (Z. Lai), hlinch@mail.sysu.edu.cn (L. Huang), mingdfenglei@csu.edu.cn (M. Lei).

https://doi.org/10.1016/j.engfracmech.2023.109171
Received 23 November 2022; Received in revised form 28 January 2023; Accepted 28 February 2023

1. Introduction

Heterogeneous materials that contain irregular inclusions are frequently encountered in engineering activities [65,3]. With proper treatment, heterogeneous materials provide useful and practical functionality. For instance, rock blocks mixed with clay soil can be used as an effective material to construct pavement or railway substructures [33]. In geotechnical engineering, heterogeneous geomaterials with irregular inclusions are found under various conditions, such as mine waste dumps, conglomerates of dam material tailing, other conglomerates, glacial tills, track-bed materials, soil rock mixtures, rock fills, breccias and tectonic mélanges [33,40]. These common geomaterials are abundant and widely distributed in nature. The utilization of these useful materials has the potential to save money and reduce energy consumption during engineering construction [69,68,50]. To realize this potential, it is essential to understand the mechanical properties of heterogeneous geomaterials, which are dominated by internal structures and interactions among the internal components. Thus, there has been much research on the physical and mechanical properties of heterogeneous materials in recent decades.

Conventional geotechnical experiments have been conducted extensively to investigate quantitative relationships between mechanical properties and internal structure characteristics, i.e., inclusion contents, shapes, and gradations [37,66,62,3,64,31]. Despite these research efforts, the micromechanical behaviours and failure characteristics of heterogeneous rocks cannot be explicitly observed during conventional shearing or compression tests. The X-ray computed tomography (CT) technique offers a powerful solution to investigate the deformation and failure characteristics of heterogeneous geomaterials [12,13]. By combining uniaxial and triaxial compression tests, the damage evolution and fracturing mechanism of heterogeneous geomaterials with various internal structures have been investigated using a CT procedure [37–38,44]. However, the scale of the specimens examined in CT experiments has been quite limited, usually ranging from 10 mm to 50 mm [12,40]. In addition, CT experiments are costly, and the experimental operations and digital image processing are complicated, which limits the applications of CT experiments in engineering projects.

With the advancement of computer science, numerical approaches have been developed rapidly in recent years. Such approaches have become a practical and promising alternative or supplement to physical experiments. A considerable number of numerical investigations have been conducted to investigate the mesoscale mechanical responses and failure characteristics of heterogeneous geomaterials using the finite element method (FEM) [65,65,15–16,16] extended finite element method (XFEM) (Belytschko and Black, 1999 [1]), discrete element method (DEM) [8,7,4,58,60], discontinuous deformation analysis (DDA) [9,24] and finite discrete element method (FDEM) [47–50,29]. These methods can be used in combination with detailed reconstructions of stochastic internal structures to conveniently and clearly show mesoscale mechanical and failure propagation processes in heterogeneous geomaterials.

Li et al. (2020) [14,18] combined the level set method (LSM) and permeability-based hydraulic fracturing (PHF) model with the FEM to model the hydraulic fracturing characteristics of heterogeneous strata. Zhang et al. [63,65] (2021) considered the effects of inserting spherical inclusions and systematically investigated the mesoscopic dynamic and static responses of heterogeneous materials in two and three dimensions. Zhao et al. (2021) [67] extracted realistic inclusion contours from digital images of a disordered stratum and established a framework to generate a numerical model of the stratum. The concept of an equivalent fracturing zone was defined to trace failure propagation in these studies and applied as a classical solution for failure analysis using traditional FEM [65], Li et al. (2020) [18]. Realistic discontinuous cracking behaviours cannot be modelled using the conventional FEM. The XFEM can successfully address the numerical singularities across the cracks and discontinuities by coupling additional enriched functions to the standard FEM (Wu et al., 2018) [42]. However, defining the enrichment of the approximation space can be quite challenging and problematic when multiple cracks intersect, which limits the application of this approach in the study of the fracturing behaviours of heterogeneous materials, particularly those with irregular inclusions.

In recent decades, DEM has been accepted as a prevalent and promising numerical method for simulating large and discontinuous deformations. The failure process and mesoscale mechanical responses have been explicitly presented by searching, evaluating, and updating bonded states among particles [8,6,27,28]. Gong et al. [7] (2019) used clumps of bonded tiny particles to model inclusions with irregular shapes. In this way, the breakage of inclusions was modelled when the fracturing or strength criterion among the bonded particles was reached. However, using many tiny particles significantly increased calculation costs. To address this limitation, Wang P [32,35] et al. (2021) defined a new strategy to consider the breakage and failure characteristics in DEM, this strategy is called the 'new replacement model'. Multiple-scale failure, including grain breakage and bond breakage, can be simulated simultaneously through this approach [59]. However, shape effects were not included in this methodology. In addition, the fine and coarse components of heterogeneous geomaterials are continuous and homogeneous individually in many cases. Therefore, the fully discrete and discontinuous assumption may not be appropriate to characterize the intrinsic nature of geomaterials with irregular inclusions. The same dilemma was encountered during DDA analysis [9,11].

The FDEM is a hybrid numerical approach that includes the characteristics of both continuity and discontinuity. Yan et al. conducted systematic investigations on the thermal, hydraulic, and coupling fracturing behaviours of soil and rocks with stochastic initial damage [49,51,52]. Recently, Yan developed and launched an FDEM program named 'MultiFracS' [53,54]. With appropriate modelling, stochastic intersecting fractures were simulated efficiently and effectively through this FDEM program [55,43]. In addition, the effects of disordered weak planes or interfaces of heterogeneous materials were modelled conveniently by introducing a zero-thickness element [5,61,21–23]. Wei et al. [41] validated that failure patterns and characteristics of irregular particles can be accurately simulated using the FDEM. Previous research results indicated that the FDEM is an effective tool to address continuous and discontinuous deformations of heterogeneous geomaterials. Although FDEM models were extensively applied in the scientific literature, a limited number of examples efficiently replicated the microstructures of heterogeneous geomaterials, especially for those with high contents of irregular inclusions. One critical problem was that the mesh quantity and quality of the FDEM were unsatisfactory when many irregular inclusions were included. Modelling the interfaces and their fracturing behaviour among inclusions and matrices

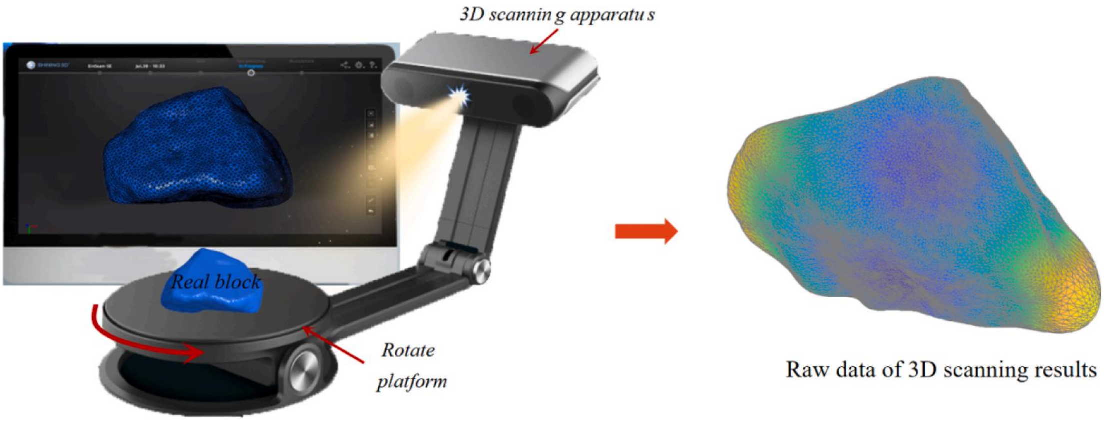

Fig. 1. Acquisition of the surface morphology of irregular inclusions using 3D laser scanning equipment.

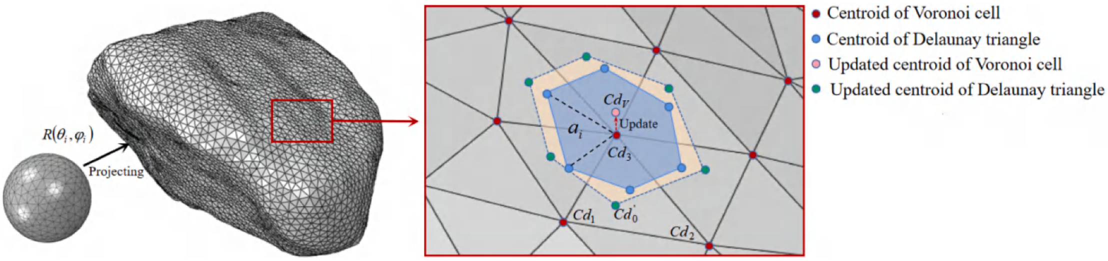

(a) Generate mesh surface weighted by the curvature

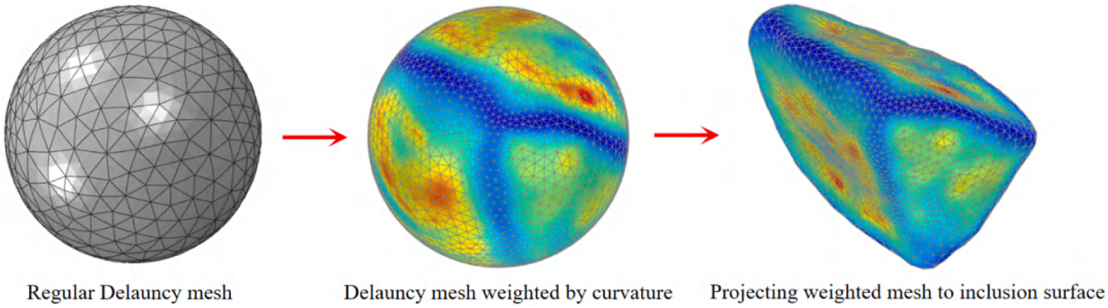

(b) Projection between parametric variables and outcome inclusion surface

Fig. 2. Detailed strategy of the CWSVM.

was difficult. Therefore, the effects of the interface properties on the mechanical properties (such as cohesion and friction angle) and fracturing characteristics were not systematically investigated [72,57].

To overcome the abovementioned limitations, this study establishes an approach to simulate heterogeneous geomaterials with irregular inclusions. First, 3D scanning techniques are employed to obtain the inclusion surface morphology. Subsequently, a computational geometry method, named the curvature-weighted sphere Voronoi method (CWSVM), is employed to refine the surface morphology and control the mesh quantity and quality. Then, the signed-distance-field-based discrete element method (SDF-DEM) is used to approximate the natural spatial distribution and orientation of inclusions. Notably, a large content of inclusions in heterogeneous geomaterials can be modelled with this approach. Next, to model the fracturing process and interface behaviour, an FDEM model is developed by integrating cohesive elements into the mesh in a fast and efficient manner. In addition, a combined constitutive model is proposed to consider the shear-hardening behaviour of the cohesive elements. Then, the developed FDEM model is verified by comparison with experimental results that range from the shape characteristics of the inclusions to the mechanical behaviour of the geomaterial. Finally, the effects of interface strength on the mechanical and fracturing behaviour of geomaterials are further investigated using the validated method.

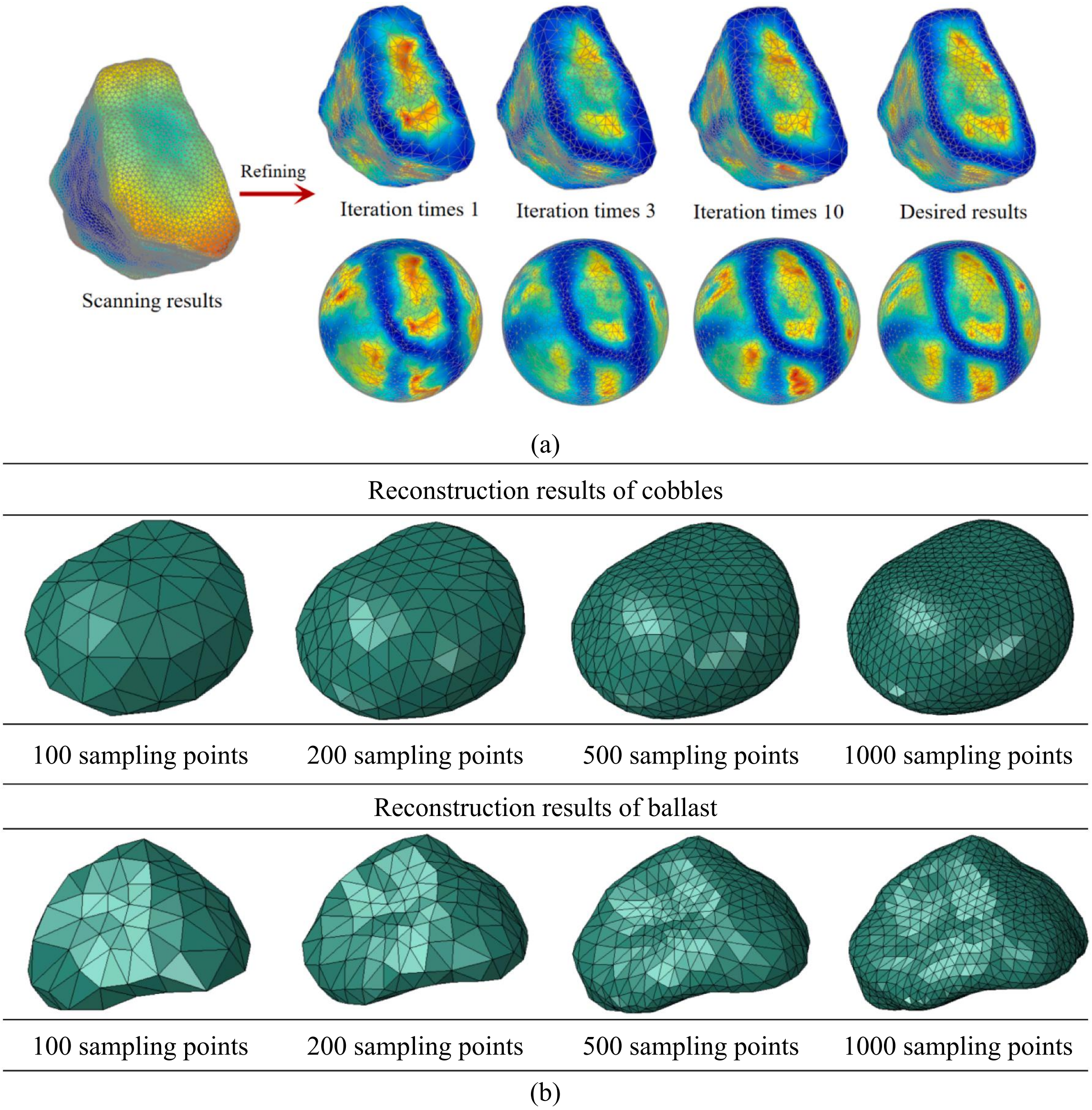

Fig. 3. Evolution of the surface of a particle during the CWSVM reconstruction process (a) and examples of reconstructed surfaces with different numbers of sampling points (b).

2. Methodologies

2.1. Control mesh quantity and quality based on the CWSVM

(1) Acquisition of the surface morphology of irregular inclusions using 3D laser scanning

To obtain the surface morphology of irregular inclusions, a 3D laser scanning apparatus is employed to generate a high-density point cloud of irregular inclusions, as shown in Fig. 1. Therefore, detailed shape characteristics of inclusion surfaces can be well replicated. However, the raw point cloud is rather indeterminate and cluttered. The inclusion geometry that is obtained directly from point clouds using Delaunay meshes is unsuitable for numerical analysis, as sharp corners and short edges would significantly increase mesh quantity and degrade mesh quality. Thus, appropriate refinements must be conducted on the surface morphology so that numerical analysis can be performed.

(2) CWSVM

As mentioned above, the accuracy, convergence, and efficiency of numerical simulations are notably affected by the mesh quantity and quality. In previous research, the corners of inclusion morphologies had greater effects than flat regions on mechanical properties [25,26]. Thus, in this study, it is inferred that calculation efficiency and accuracy can be balanced by considering corner regions in

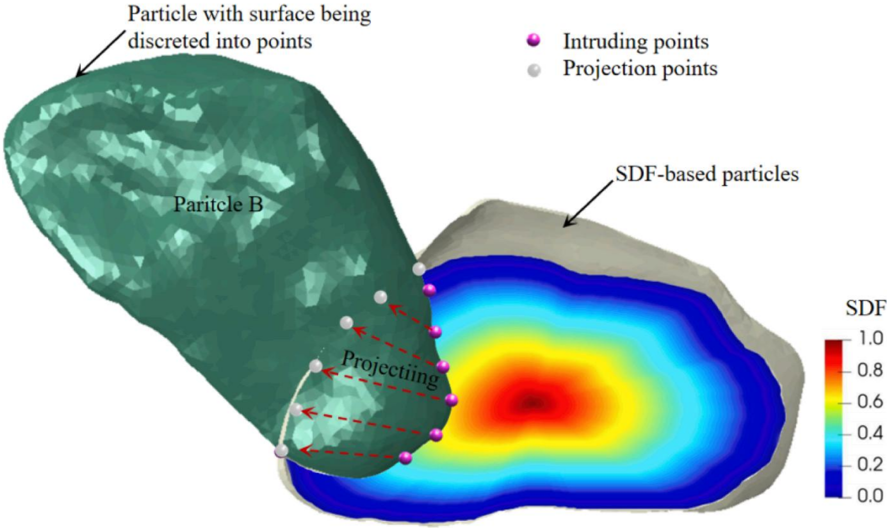

Fig. 4. Strategy of the SDF-DEM.

detail and flat regions relatively simplistically. To achieve this, a CWSVM method is originally developed to generate desired inclusion geometry with limited points and meshes. The detailed strategy is presented in Fig. 2.

To proceed with the refinement process, first, the inclusion surface is continuously presented by the sphere harmonic (SH) function [20]. For each point on a standard sphere surface (as shown in Fig. 2(a)), a corresponding projection point on the inclusion surface is easily found through the SH function. Therefore, a series of seed points on block surfaces are selected based on randomly generated points on a standard sphere. Then, the initial inclusion surface is generated using the Delaunay method, the density is controlled by the total number of seed points. Next, the desired inclusion surface is obtained by making Delaunay triangles (i.e., seed points) intensive on the corners (high curvature) and sparse on the flat regions (low curvature). To accomplish this task, a weighted index is introduced based on point curvature, which is:

$$w_{ci} = \frac{E_{ci} - \mu}{N \cdot \sigma} \tag{1}$$

where$E_{ci} = \ln(1/c_i)$, c_i is the maximum principal curvature of a seed point, and μ and σ are the average and standard deviation of all E_{ci} on block surfaces, respectively. N is the number of seed points.

As shown in Fig. 2(a), Voronoi cells have duality with Delaunay triangles. Each vertex (seed point) on the inclusion surfaces is the centroid of a Voronoi cell. A Voronoi cell is formed by connecting the centroids of nearby Delaunay triangles. Similarly, the centroid of a Delaunay triangle is a vertex of a Voronoi cell. Therefore, once the centroid of a Delaunay triangle is updated, the corresponding centroid of the Voronoi cell (i.e., a vertex on the inclusion surface) also changes. To update vertices on the inclusion surface based on curvature, the centroids of a Delaunay triangle are determined as follows:

$$dis(cd_0, cd_1, w_{c1}) = dis(cd_0, cd_2, w_{c2}) = dis(cd_0, cd_3, w_{c3}) \tag{2}$$

wherecd_0,cd_1,cd_2 and cd_3 are the coordinates of the centroid and vertices of a Delaunay triangle (as shown in Fig. 2(a)), respectively.w_{c1}, w_{c2} and w_{c3} are weighted indices of vertices; *dis* is the weighted distance function, given by:

$$dis(cd_0, cd_1, w_{c1}) = \|cd_0 - cd_1\|^2 - w_{c1} \tag{3}$$

where the symbol $\| \cdot \|$ indicates the Euclidean distance.

After the weighted centroids of the Delaunay triangle are obtained, the updated centroid of the Voronoi cell is determined and defined by:

$$cd_V = \frac{\sum_i^n a_i cd_i}{\sum_i^n a_i} \tag{4}$$

where cd_V represents the coordinates of the centroid of the Voronoi cell and cd_i represents the vertex coordinates of the Voronoi cell. a_i is the triangle area, as shown in Fig. 2(a), which is calculated using the original centroid of the Voronoi cell as a reference.

Then, the vertex is updated to a new position. All vertices on the inclusion surface are updated following the same procedure. The whole procedure is performed repeatedly until the original and updated centroids of the Voronoi cell are rather close. In this case, the desired inclusion surface covered by curvature-weighted Delaunay triangles is obtained. The updating process is illustrated in Fig. 3(a). The vertices are intensive at corners but sparse in flat regions, as expected. The reconstructed inclusion surface with various vertex

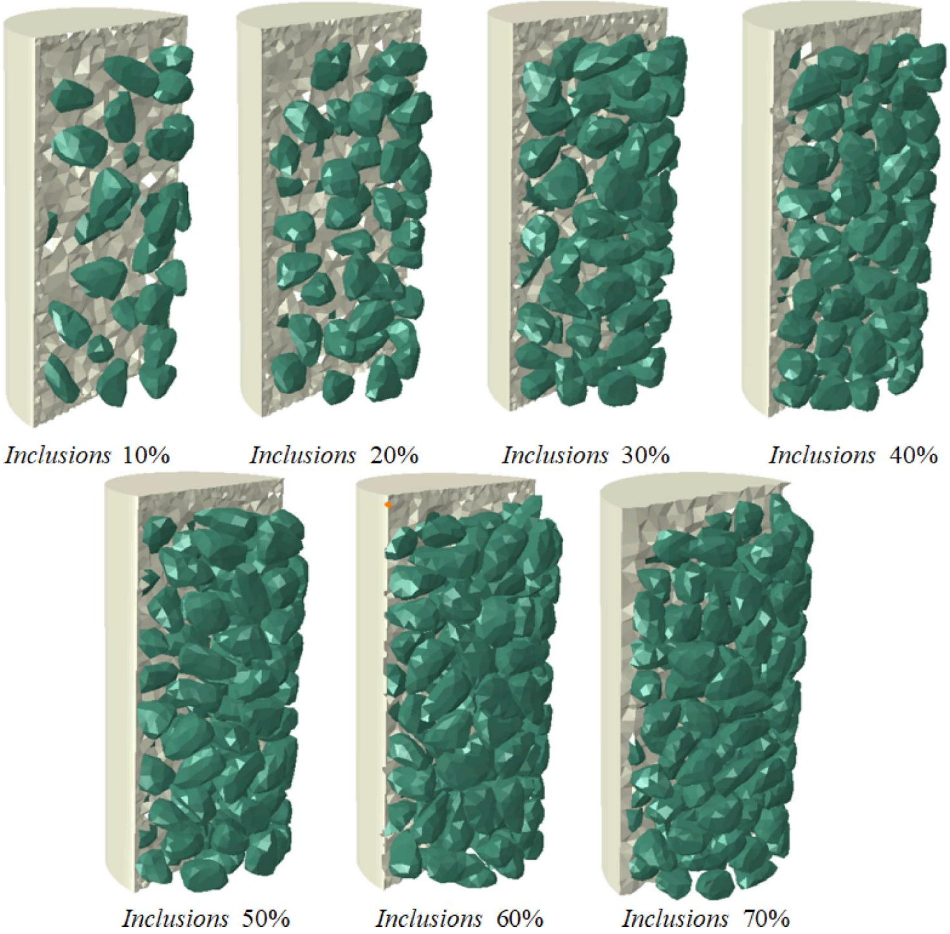

Fig. 5. Heterogeneous geomaterials with various inclusion contents.

numbers is presented in Fig. 3(b). The inclusion shape characteristics are generally retained even with a small number of vertices. In addition, the density of Delaunay triangles on the inclusion surface gently changes the following curvature for each case. Both the quantity and quality of Delaunay triangles are well-controlled using the proposed method.

2.2. Generation of 3D heterogeneous specimens with controlled features using SDF-DEM

Allocating irregular inclusions in a specific region is a critical step for the generation of heterogeneous specimens. It is rather difficult and time-consuming to create specimens with large contents of inclusions, even though some computational algorithms, such as the lattice search algorithm [10] and the bounding box method [46,21], were developed to accelerate detection of overlap. To develop a model that approximates the natural spatial distribution and orientations of block inclusions and accelerate the allocation process, especially for specimens with many inclusions, a discrete element method-based numerical approach is first employed to determine the positions of block inclusions. In particular, a signed-distance-field-based discrete element method (SDF-DEM) which is a novel numerical method developed by our own [14] is combined organically in the proposed algorithm. Overlap detection and block allocation strategy under SDF-DEM are briefly introduced in Fig. 4. As shown in Fig. 4, a signed distance field (SDF) inside particle A is generated according to the radial distance from the query point to the particle surface. Since the particle surface has been continuously presented using the SH function, the signed distance function is defined as follows:

$$F(X_q) = r(\theta_P, \phi_P) - \|X_q\| \tag{5}$$

where $\|X_q\|$ represents the radial distance from a query point to the centroid of particle A and $r\left(\theta_p, \phi_p\right)$ represents the radial distance from a projection point of the query point on the particle surfaces to the centroid point, which is easily obtained from the SH function.

On this basis, the signed distance is positive inside particles and negative outside particles, and the zero value of the SDF represents the particle surface. Therefore, the contact status and overlap between two particles are easily accomplished by checking the distance signs of the surface nodes. The contact resolutions, including the contact geometric features and contact normal forces, are derived

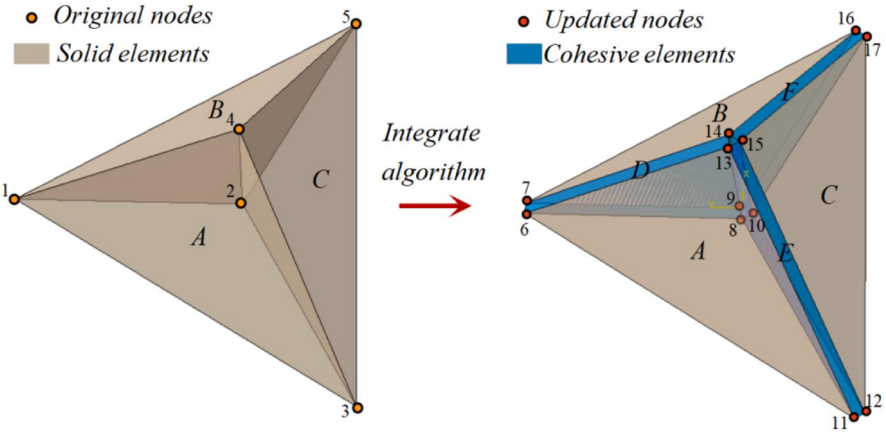

(a) Basic strategy of element coupling

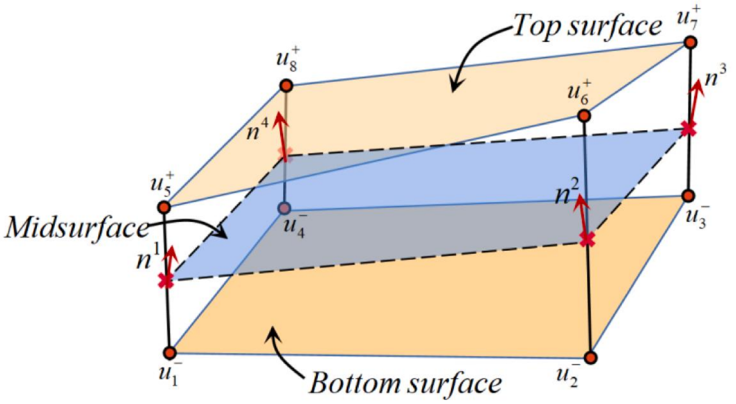

(b) Normal and shear direction computation for cohesive elements

Fig. 6. Insertion method and structural characteristics of cohesive elements.

from the distance-potential-based energy-conserving contact theory in DEM, in which the linear-spring model with Coulomb's law is adopted. More details are provided by Lai et al. [13,14]. After resolving the contact status through SDF-DEM, the position of a new particle is determined.

To generate a specimen with desired characteristics, a systematic procedure is designed to approach the natural structure of heterogeneous geomaterials. The steps in the process are as follows.

Since the aspect ratio and roundness have great effects on the mechanical and fracturing responses of the heterogeneous materials, the block morphology that has shape characteristics (i.e., aspect ratio and roundness) similar to the target objects should be obtained first for accurate modeling.

Taking a cylindrical container as an example, the volume of total blocks is determined based on a given inclusion content and container volume. By referring to the inverse transform sampling (ITS) method proposed in the authors' previous research [20], the volume of each irregular inclusion is obtained. Then, the chosen inclusions are scaled accordingly.

The obtained inclusions are then allowed to pile up under the force of gravity and form a random packing using the proposed SDF-DEM approach. With another scaling factor, blocks are enlarged and rebalanced until the height of block packing reaches the top of a container.

After obtaining inclusion packing, each inclusion is shrunk by the same scaling factor while retaining the inclusion centroid to approach the desired inclusion content. In this way, the orientations and spatial distributions of blocks are determined by gravity and friction, similar to those of natural heterogeneous geomaterials. Seven examples of established models are presented in Fig. 5. Heterogeneous geomaterials that contain many block inclusion (such as 60 % and 70 %) are obtained effectively and efficiently through this approach.

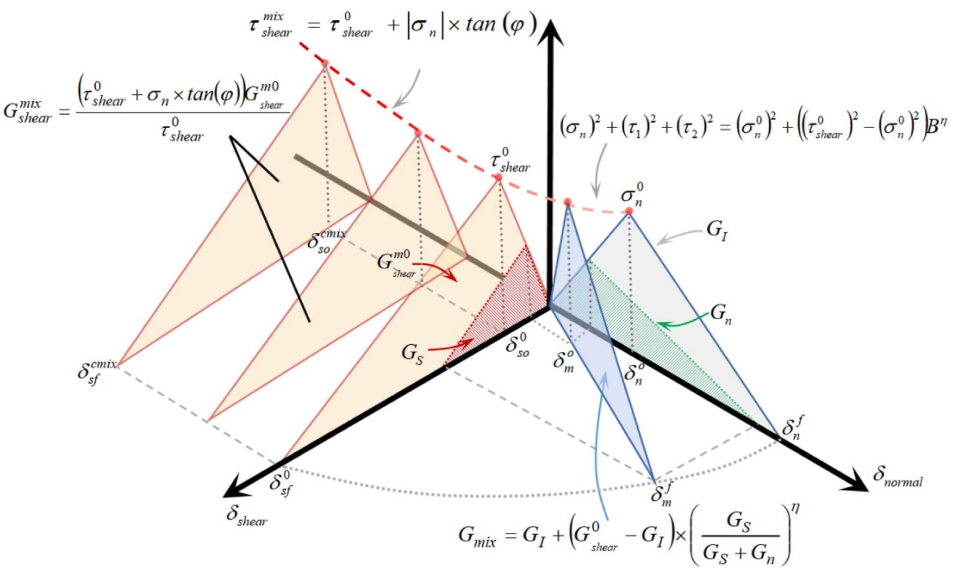

Fig. 7. Combined constitutive model of cohesive elements.

2.3. Generation of the FDEM numerical model using cohesive elements

(1) Integration of cohesive elements with finite element meshes.

To trace the fracturing and interface behaviours of heterogeneous geomaterials, zero-thickness cohesive elements are employed to generate a coupled numerical model; this is achieved by integrating them into finite element meshes. One simple example consisting of three tetrahedral elements is illustrated in Fig. 6(a). There are three shared inner faces among the solid elements. The shared faces are considered potential fracture paths, which should be identified and inserted with cohesive elements in the proposed FDEM model. Thus, crack initiation and propagation in the continuum is simulated through cohesive element breaking. The basic strategy of cohesive element generation is to replicate and renumber element nodes on the shared faces (i.e., nodes 1–5 in Fig. 6(a)) but retain their original coordinates. Taking Node 4 in Fig. 6(a) for instance, Node 4 is replicated and replaced by Nodes 13–15, but Nodes 13–15 share the same coordinate as Node 4. Node replication times are determined by the number of connected elements. The same procedure is conducted for the remaining nodes on the shared element faces. Then, cohesive elements are generated using the newly updated nodes. Taking element D in Fig. 6 as an example, it is composed of node sequence 6-13-8-7-14-9. Since node pairs share the same coordinates, generated cohesive elements also have zero thickness. The thickness of the cohesive elements in Fig. 6 is exaggerated for clarity. No triangle gap exists among the nodes 13–15 at the very beginning, while the gap would be formed with the fracturing process.

However, with increasing numbers of nodes and elements, updating node and element numbers becomes quite complicated and challenging. To efficiently accomplish this updating process in Abaqus, a Python script is developed; the details are provided in Lin et al. [17,21].

(2) Deformation transition between cohesive elements and solid elements

Initially, the top surface of a cohesive element overlaps with the bottom surface, as shown in Fig. 6(b). With increasing external loading and deformation of adjacent elements, the top and bottom surfaces are no longer coincident with each other, resulting in deformations of the cohesive element. The displacement vector δ at one node pair is expressed as:

$$\delta = u_i^+ - u_j^- \tag{6}$$

where u_i^+ is the node displacement on the top surface and u_j^- is the node displacement on the bottom surface.

To analyse the mechanical responses of cohesive elements, the displacement vector should be decomposed into both normal and tangential directions within the cohesive element, as illustrated in Fig. 6(b). To obtain the normal direction of the cohesive element, a mid-surface is defined and computed by averaging the coordinates of the node pairs forming the bottom and top surfaces of the cohesive elements. Then, the normal direction is obtained as the cross-product of two tangent directions. Thus, the normal opening amount δ_N and tangential slippage amount δ_T in the cohesive element are expressed as:

$$\begin{cases} \delta_N = \delta \cdot n \\ \delta_T = \delta \cdot t \end{cases} \tag{7}$$

where n and t are normal and tangential directions within a cohesive element.

Then, the mechanical and damage responses of the cohesive elements follow the constitutive cohesive zone model.

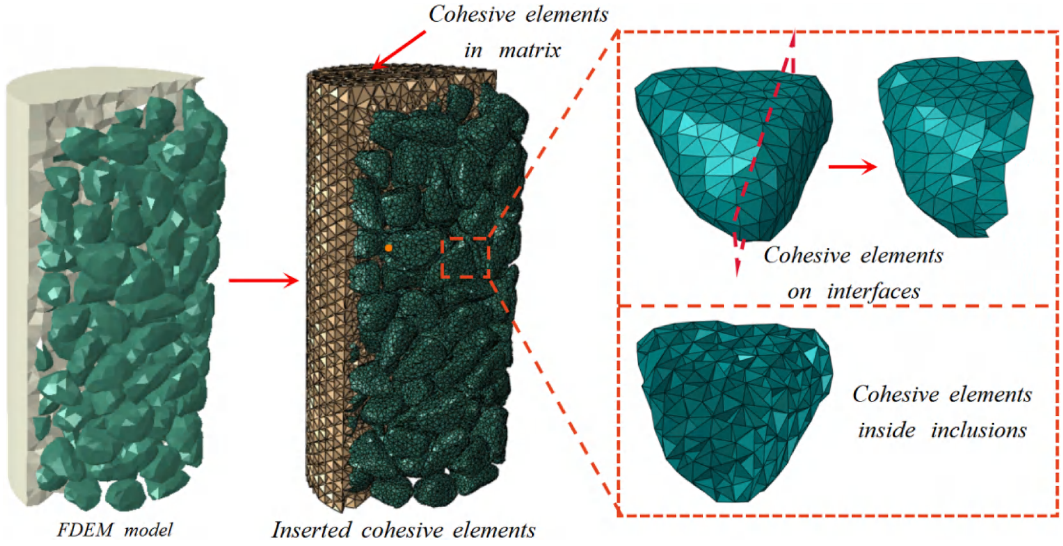

Fig. 8. FDEM model for heterogeneous geomaterials.

(3) A combined cohesive zone model

Previous studies have shown that the mode-II fracture toughness of limestone is sensitive to the confining pressure. The mode-II fracture toughness increases from 1.78 MPa·m to 14.49 MPa·m with an increase in the confining pressure from 0.1 to 40 MPa [46,44,36,35,36]. However, the shear strength and fracture energy of a cohesive element remain constant when it is under compression in the conventional model. To consider the shear-hardening behaviours of geo-materials (especially for those under high confining pressure), the new cohesive zone model is developed in this study, which is illustrated in Fig. 7.

Since the Mohr-Coulomb criterion is widely accepted as an effective method to describe shear hardening behaviours, it is employed to predict the shear strength. When normal stress$\sigma_n < 0$, the relation between the shear strength and compression stress of a cohesive element is assumed to follow:

$$\tau_l^i = \tau_l^{i0} + |\sigma_n| tan\phi \quad i = 1,\ 2 \tag{8}$$

where σ_n is the normal stress, ϕ is the friction angle, τ_l^{i0} is the original shear strength when σ_n equals zero, and τ_l^i represents the hardening strength in the shear direction.

Then, the shear opening and fracture displacement (i.e., δ_{so}^{har} and δ_{sf}^{har} in Fig. 7) are defined to obtain a complete constitutive model under the compression state. According to previous experiments on geomaterials, the shear opening and fracture displacement of geomaterials are much less sensitive to the confining pressure than the shear strength (Yin et al., 2021) [24]. It is acceptable to set them as constants against various confining pressures (Fig. 7), as adopted extensively in published research [46] (Wang et al., 2021). Thus, the fracture toughness G_{shear}^i and stiffness k_{shear}^i in the shear direction are presented as:

$$\begin{cases} G_{shear}^i = \dfrac{\left(\tau_l^0 + |\sigma_n| \times (tan\phi)\right) G_{shear}^{i0}}{\tau_l^0} \\ k_{shear}^i = \left(1 + \dfrac{|\sigma_n| \times (tan\phi)}{\tau_l^0}\right) \times k_{shear}^{i0} \end{cases} \quad i = 1,\ 2 \tag{9}$$

where G_{shear}^{i0} and k_{shear}^{i0} are the original fracture toughness and stiffness in the shear direction when σ_n equals zero.

For$\sigma_n > 0$, Benzeggagh and Kenane [2] (1996) proposed a classic expression for the mixed critical energy release rateG_{mix}, which is:

$$G_{mix} = G_I + \left(G_{shear}^{m0} - G_I\right) \times \left(\frac{G_S}{G_S + G_n}\right)^{\eta} \tag{10}$$

where G_I and G_{shear}^{m0} are the pure mode fracture toughness values under tensile and shear stress, respectively. Note that$G_{shear}^{m0} = G_{II} + G_{III}$. G_n and G_S are the tensile and shear fracture toughness in mixed mode, as shown in Fig. 7.

Regarding the criterion for delamination initiation, Turon et al. [30] proposed a criterion that evolves the propagation criterion and the damage evolution law:

$$(\sigma_n)^2 + (\tau_1)^2 + (\tau_2)^2 = \left(\sigma_n^0\right)^2 + \left(\left(\tau_{shear}^0\right)^2 - \left(\sigma_n^0\right)^2\right) B^{\eta} \tag{11}$$

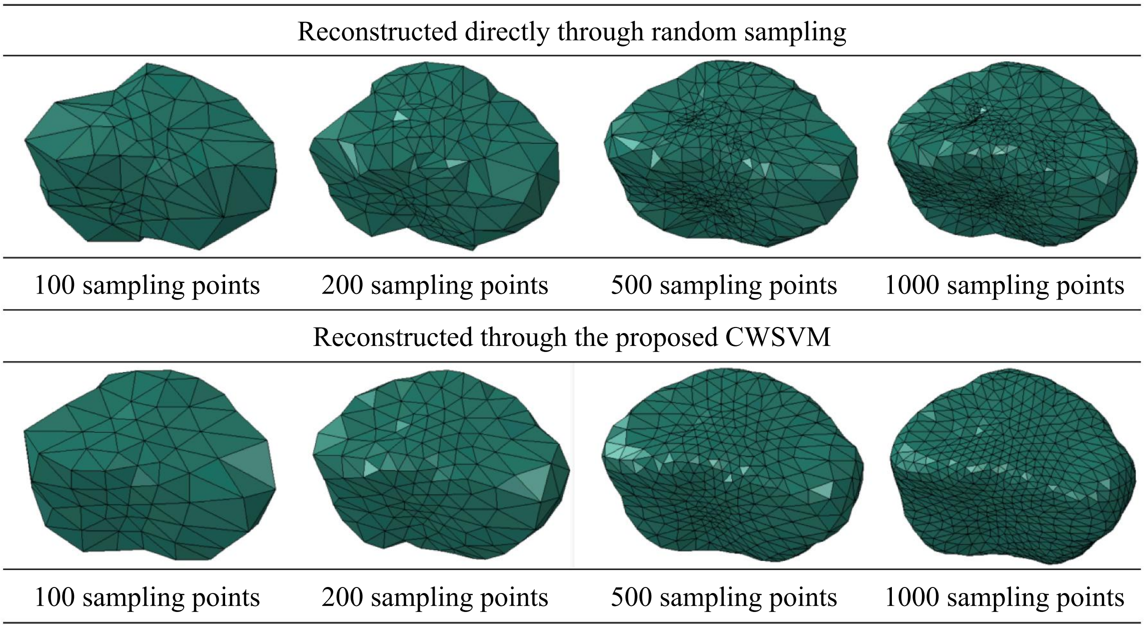

Fig. 9. FDEM model for heterogeneous geomaterials with various inclusion fractions.

where$\left(\tau^0_{shear}\right)^2 = \left(\tau^1_l\right)^2 + \left(\tau^2_l\right)^2$,$B^\eta = G_s/(G_s+G_n)$, which was calculated by:

$$B = \frac{\beta^2}{1+2\beta^2-2\beta}\ ,\beta = \frac{\delta_{shear}}{\delta_{shear}+\delta_n} \tag{12}$$

where δ_{shear} and δ_n are the shear and normal displacements and$\delta_{shear} = \sqrt{\delta_s^1 + \delta_s^2}$.

Based on Equation (13), the mixed-mode onset displacement δ^o_{mix} and stiffness k_{mix} are determined as follows:

$$\begin{cases} \delta^o_{mix} = \sqrt{\left(\delta^o_{shear}\right)^2 + \left(\left(\delta^o_{shear}\right)^2 - \left(\delta^o_n\right)^2\right)B^\eta} \\ k_{mix} = k_n(1-B) + k_{shear} \times B \end{cases} \tag{13}$$

On this basis, the mixed-mode behaviours of cohesive elements ($\sigma_n > 0$) are determined. The combined shear hardening constitutive model is presented in Fig. 7.

When a cohesive element completely degrades, the cohesive element is deleted to introduce true cracks in the sample domain. Since the bottom and top surfaces of a cohesive element share the same surfaces of a neighbouring element, the shared surfaces are reactive if the cohesive element fails. Then, the active surfaces are included in the general contact definition, which adopts the classic Coulomb friction model. Then, a user-defined subroutine that defines constitutive law (i.e., VUMAT) is developed to implement the constitutive law of the established combined cohesive zone model in the Abaqus/Explicit solver. A brief introduction to the VUMAT programming process is presented in Appendix A. Finally, a novel and systematic approach for modeling heterogeneous geomaterials with controllable internal structures is established by integrating the above methodologies, as shown in Fig. 8.

3. Validation of the CWSVM-based reconstruction approach and FDEM numerical method

3.1. Validation of the proposed CWSVM

In this section, the reconstructed surface morphology of inclusions using the CWSVM is examined through geometry analysis. The aspect ratio and roundness of reconstructed inclusion surfaces are used as critical indices to evaluate the efficiency of the proposed CWSVM. The calculation method of the aspect ratio and roundness are given in the author's previous work [20]. In addition, to demonstrate the advances of the proposed CWSVM, another group of inclusion morphologies is reconstructed directly through random sampling points on the inclusion morphology, as shown in Fig. 9.

The relative errors of the aspect ratio and roundness are obtained by comparing the reconstructed inclusion morphology with the original morphology obtained from 3D laser scanning for both groups. The results are illustrated in Fig. 10, wherein five different rock blocks have been tested. The relative errors of both the aspect ratio and roundness decrease notably with the increasing number of sampling points. In each case, the inclusion morphologies reconstructed using the proposed CWSVM are generally closer than those

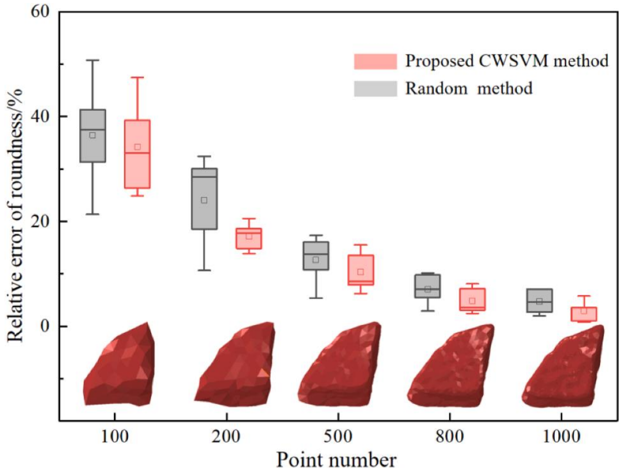

(a) Comparison of roundness

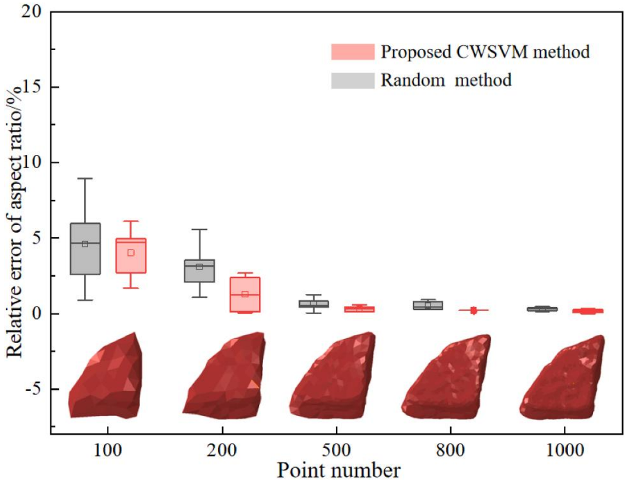

(b) Comparison of aspect ratio

Fig. 10. Comparison of shape characteristics from the random and proposed CWSVMs.

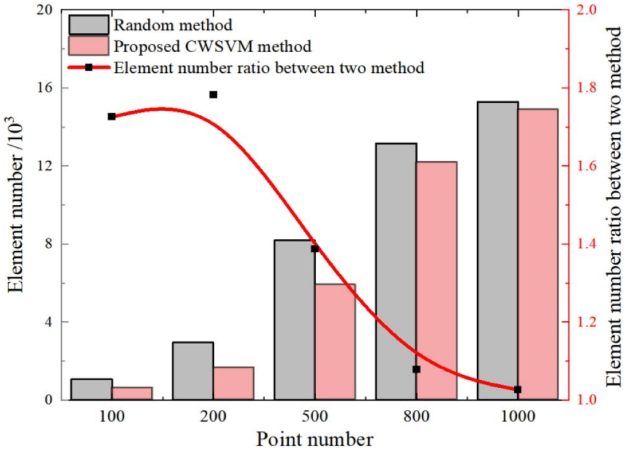

Fig. 11. Comparison of element numbers obtained using the two methods under the premise of the same shape representation accuracy.

Table 1
Mechanical parameters of the experiments and numerical models.

Mechanical parameters	Rocks	Matrix	Cohesive elements	
			Matrix	Interface
Elastic modulus (MPa)	20,000	6.6	—	—
Poisson's ratio	0.22	0.3	—	—
Friction angle (°)	—	16	—	—
Cohesion(kPa)	—	60	—	—
Tensile stiffness (GPa/m)	—	—	700	400
Shear stiffness (GPa/m)	—	—	160	100
Tensile strength (kPa)	—	—	20	16
Shear strength (kPa)	—	—	65	50
Shearing opening (mm)	—	—	0.85	0.7
Fractured displacement (mm)	—	—	1.45	1.1

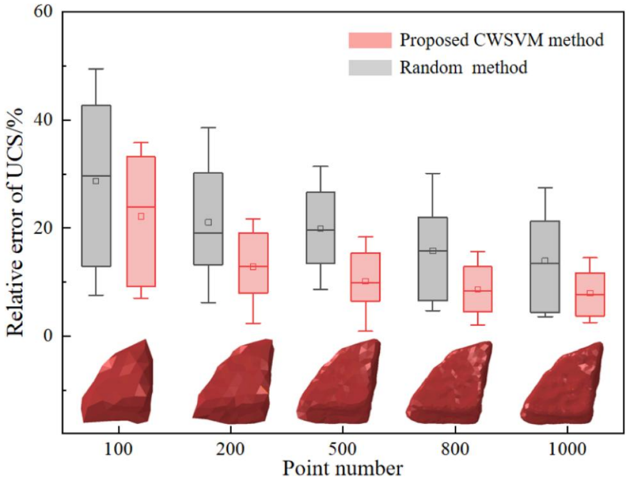

Fig. 12. Comparison of UCS values from the two reconstruction methods.

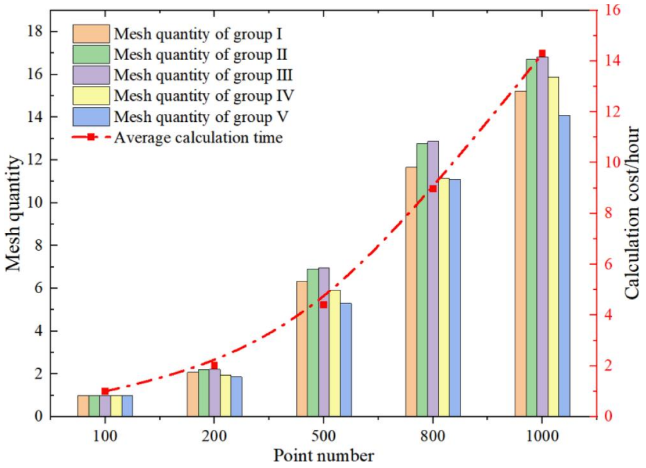

Fig. 13. Mesh quantity and calculation time of various point numbers.

obtained directly from the random method to the original inclusion morphology. When the sampling number decreases from 500 to 200, the inclusion morphologies reconstructed using the proposed CWSVM are still closer than those generated using the random method (which varied significantly) to the original inclusion morphology. In addition, comparing the relative errors in Fig. 10 (a) and (b) shows that the roundness is much more sensitive than the aspect ratio to changes in the number of sampling points. It is inferred that the curvature-weighted reconstruction strategy is necessary and effective.

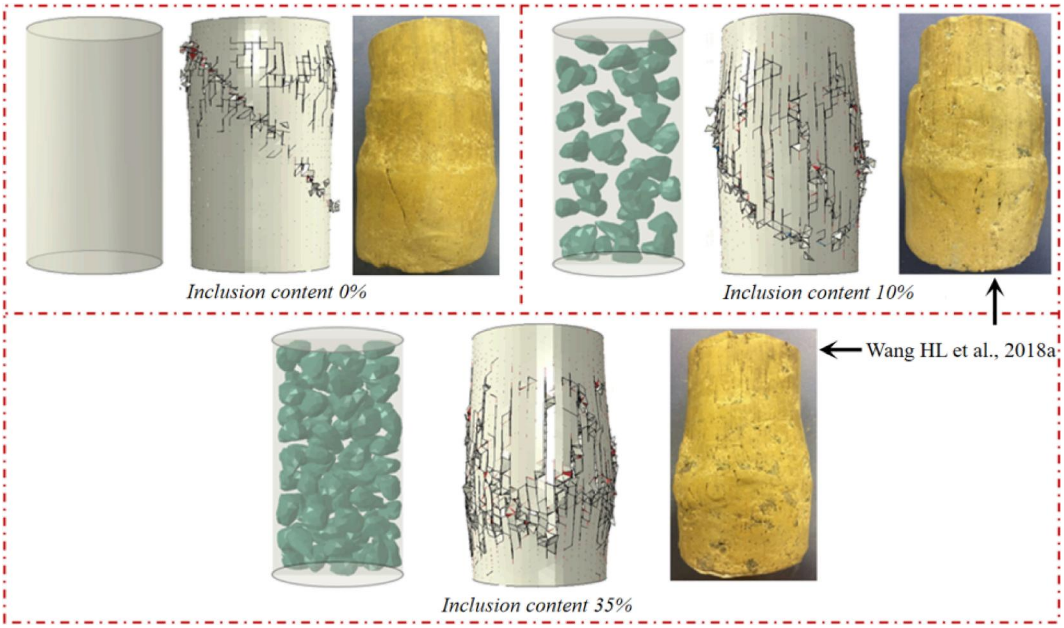

Fig. 14. Comparison of numerical results and experimental results (Wang et al., 2018a).

The comparisons of element numbers between the two methods are presented in Fig. 11. The element number ratio represents the element number obtained from the random method divided by that obtained from the CWSVM. As the sampling number is greater than 500, the element numbers generated by the two methods are rather similar. The element number ratios are less than 1.1. However, when the sampling number is less than 500, the element number generated by the random method is almost twice of that generated by the proposed method. This indicates that many more elements are needed when using the random reconstruction method to approach the same shape representation accuracy as that of the CWSVM method proposed in this study. Since hundreds of particles must be generated during the numerical analysis, the random method would lead to much lower calculation efficiency than the proposed CWSVM, which can reduce the number of mesh elements and thus improve the computational efficiency.

Next, ten groups of numerical uniaxial compression tests are conducted on cylindrical specimens (50 mm × 100 mm) using these various irregular inclusions with a consistent gradation and an inclusion content of 35 %. The mechanical parameters of the numerical model are listed in Table 1. A comparison of the uniaxial compression strength (UCS) between the two kinds of reconstruction strategies is presented in Fig. 12. The compression strength decreases notably with the increasing number of sampling points. The rate of decrease tends to be stable when the sampling number exceeds 200. Based on previous research, increasing the roundness and aspect ratio of block inclusions notably improves the mechanical strength of heterogeneous geomaterials. It is inferred that using an oversimplified inclusion morphology leads to an overestimation of the mechanical strength of heterogeneous geomaterials, as the roundness and aspect ratio increase significantly in these cases. However, using the proposed reconstruction strategy, the overestimation issue is largely mitigated. The average relative errors of compression strength are within 10 % even when the number of sampling points is reduced to 200, which is much less than the errors obtained from reconstructions generated by the random method.

The mesh element number and computational cost of the proposed CWSVM reconstruction strategy using various sampling points are presented in Fig. 13. The mesh quantity represents the total element number of the rock block divided by the element number generated using the proposed CWSVM method with 100 points. For each number of points, five groups of mesh quantities and calculation costs are investigated. With the increase in the number of sampling points, both the mesh quantity and calculation time improve notably, especially when the sampling number exceeds 200. Using limited sampling points to reconstruct the inclusion surface but retain critical shape features significantly reduces mesh quantity and calculation costs while retaining calculation accuracy. The results indicate that the proposed CWSVM can be used as an effective tool to balance the efficiency and accuracy of the hybrid numerical model.

3.2. Comparison with experimental results in available research

To further validate the accuracy of the proposed FDEM approach, comparisons between FDEM modelling and experimental results are conducted. Wang et al. [33] conducted a systematic study on composite geomaterials with various contents of included coarse grains. They performed triaxial compression tests on fabricated specimens with the drainage value open. For each kind of specimen, shearing at a constant axial strain rate of 0.5 mm/min was conducted. The tests ended after the axial strain reached 15 %, at which point failure occurred. Three kinds of specimens with 0 %, 10 %, and 35 % inclusion contents from their study are illustrated in Fig. 14 after shearing at a confining pressure of 30 kPa. In the present study, corresponding numerical models of consistent inclusion contents

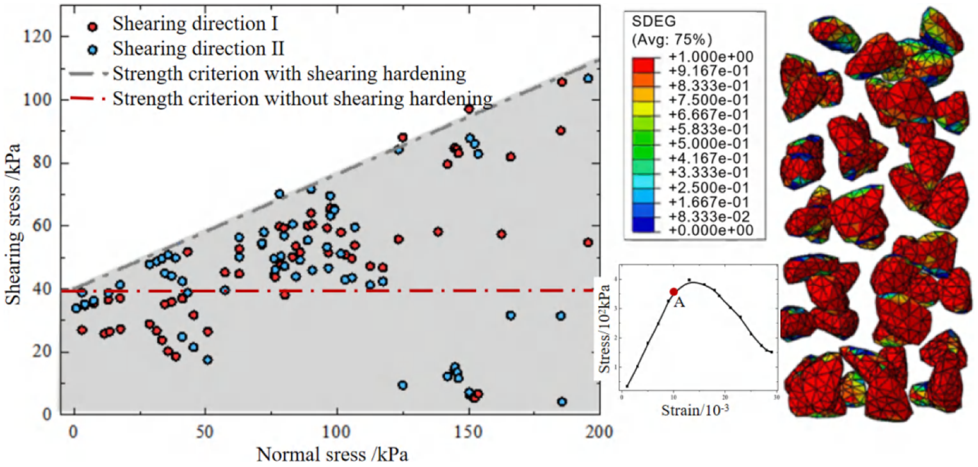

Fig. 15. Stress state of cohesive elements at interfaces.

are developed, and numerical triaxial compression tests are conducted on the specimens with loading conditions the same as those in the laboratory experiments of references [32,39]. The results for both the physical and mechanical parameters from the experiments and numerical models are illustrated in Table 1. Some basic mechanical parameters, such as cohesion and friction angle, are directly obtained from the literature [32,39]. In addition, stress–strain curves of specimens with 0 % inclusion contents from the literature [32,39] are employed to calibrate the mechanical parameters of the matrix. Notably, a series of trial and error efforts are conducted to calibrate the mechanical parameters of the interfaces. Details are available in the authors' previous research [20,21]. Since the mechanical strength of hard inclusions is significantly greater than that of the matrix, it is unlikely that hard inclusions fracture during triaxial compression tests at low confining pressures. Thus, the hard inclusions in the numerical models are considered homogeneous and elastic.

The failure characteristics of the numerical and experimental results are compared in Fig. 14. A clear shearing band and limited dilatancy are observed for both numerical and experimental specimens with an inclusion content of 0 %. As the inclusion content increases to 10 %, dilatancy becomes more pronounced. Additionally, various fracture paths are observed on the surface of the numerical specimen. With a further increase in the inclusion content, the failed specimen expands notably in the radial direction in both the numerical and experimental results. Fracture paths are much more disordered and irregular compared to that of the specimen with no inclusion. It is inferred that randomly distributed hard inclusions significantly block and change the stress transfer and fracture processes, which leads to distinctive mechanical behaviours. Overall, the good agreement of the numerical and experimental results indicates the capability of the proposed method for modelling the fracturing behaviours of heterogeneous geomaterials.

Since interfaces are the most vulnerable components in heterogeneous geomaterials, the most cohesive elements on the interface are the first to reach the failure criterion during the compression process, as shown in Fig. 15, wherein the SDEG represents the scalar stiffness degradation. The stress states of unit cohesive elements that are about to fracture are presented on the left in Fig. 15. Unlike the traditional shearing criterion (red dashed line in Fig. 15), the shearing stress grows almost linearly as the normal stress increases. In addition, the stress state for each unit cohesive element is well controlled within the defined shear hardening criterion. This indicates that the developed VUMAT program works effectively for compression analysis.

The mechanical strength of heterogeneous geomaterials is predicted using the proposed method. A comparison of the mechanical strengths between the numerical and experimental results with various confining pressures is presented in Fig. 16. As shown in Fig. 16 (a), the stress–strain curves were similar between the experimental and numerical results in general, particularly for the elastic portions. Notable increases in compression strength are observed with increasing inclusion contents. The post-peak behaviours for all inclusion contents were observed as ductile and strain softening. The comparison of mechanical strength is presented in Fig. 16(b). With increasing confining pressure and inclusion content, compression strength grows up non-linearly in both numerical and experimental results, as shown in Fig. 16(b). Notably, the experimental results are slightly higher than the numerical test results. It may be caused by the inconsistency of the grain size distribution in the numerical model, since tiny block inclusions are not considered, and they are homogenized into the matrix following previous research [64]. However, in general, the numerical results share similar evolution trends with the experimental tests. The effects of the confining pressure and inclusion content on the mechanical strengths of heterogeneous geomaterials are well simulated, which validates the effectiveness of the proposed hybrid numerical method.

4. Effects of interface strength on mechanical and fracturing behaviours

As mentioned in Section 3.2, the interfaces between the matrix and inclusions are the most sensitive components of heterogeneous geomaterials. Interface strength imposes significant influences on mechanical properties and interactions among internal components, especially for those with cemented matrices, such as frozen gravelly soil, volcanic rocks, and breccia. To ensure the safety of engineering activities, it is critical to understand their mechanical and fracturing characteristics with full consideration of their internal

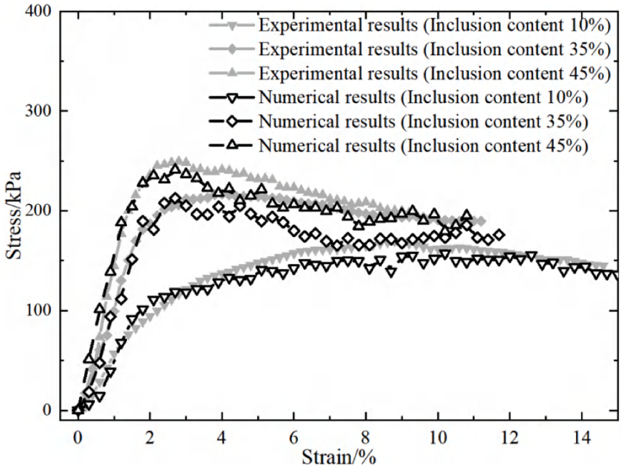

(a) Comparisons of stress-strain curves (confining pressure 30kPa)

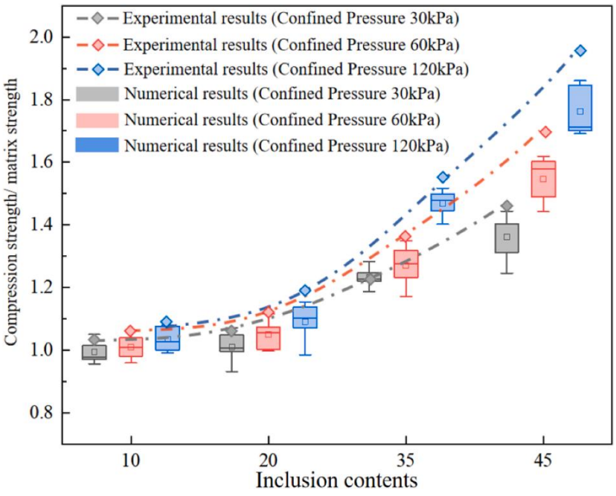

(b) Comparisons of mechanical strength

Fig. 16. Comparison between numerical and experimental results.

Table 2
Mechanical parameters of the numerical models.

Mechanical parameters	Rocks	Matrix	Cohesive elements	
			Matrix	Rocks
Elastic modulus (MPa)	35,000	6000	—	—
Poisson’s ratio	0.22	0.3	—	—
Friction angle (°)	—	32	—	—
Tensile stiffness (GPa/m)	—	—	3500	25,000
Shear stiffness (GPa/m)	—	—	800	8000
Tensile strength (kPa)	—	—	1.5	3.5
Shear strength (kPa)	—	—	2.5	12
Mode-I fracture energy (N/m)	—	—	85	150
Mode-II fracture energy (N/m)	—	—	140	300

structure and interface behaviours. Therefore, in this section, a series of sensitivity analyses are conducted to quantitatively investigate the interface effects on the mechanical and fracturing responses of these heterogeneous geomaterials with cemented matrices.

A total of 28 groups of hybrid numerical models that consider various interface strengths (20 %~140 % of the matrix strength) and

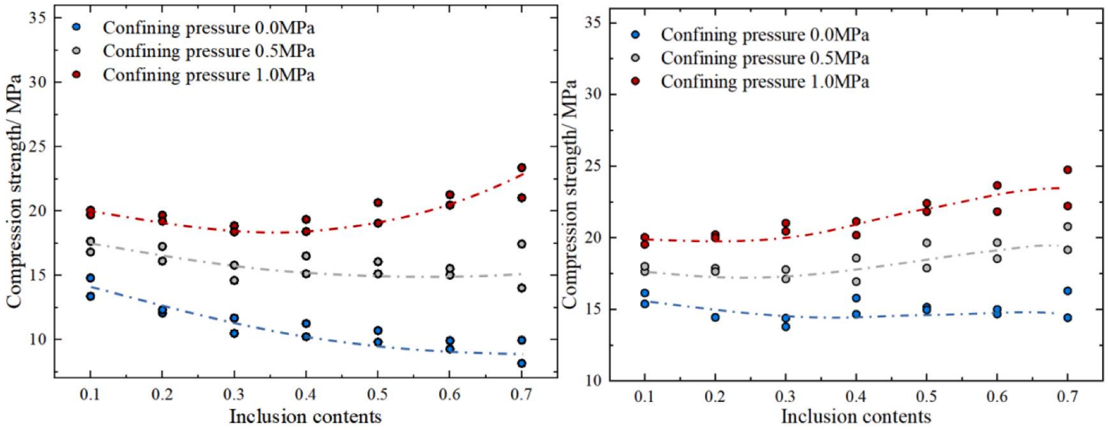

(a) Interface strength 20%

(b) Interface strength 60%

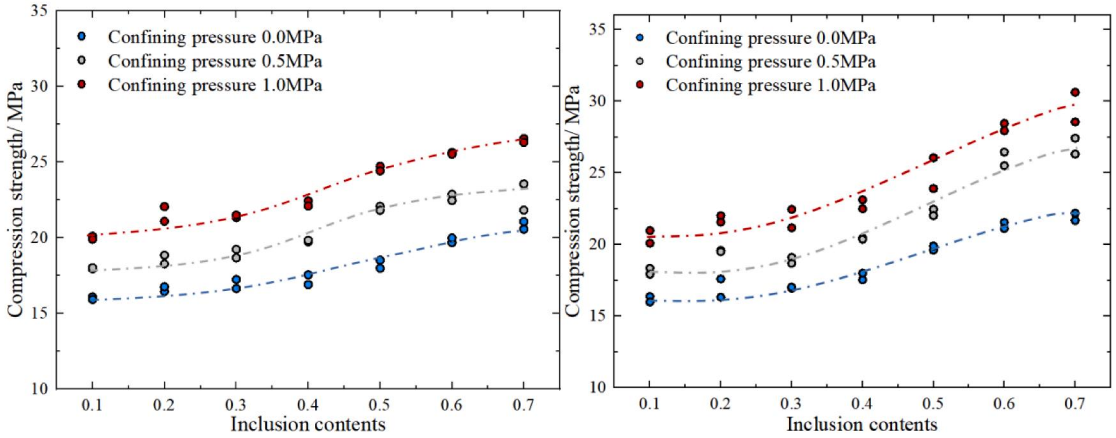

(c) Interface strength 100%

(d) Interface strength 140%

Fig. 17. Evolution of compression strength versus inclusion contents.

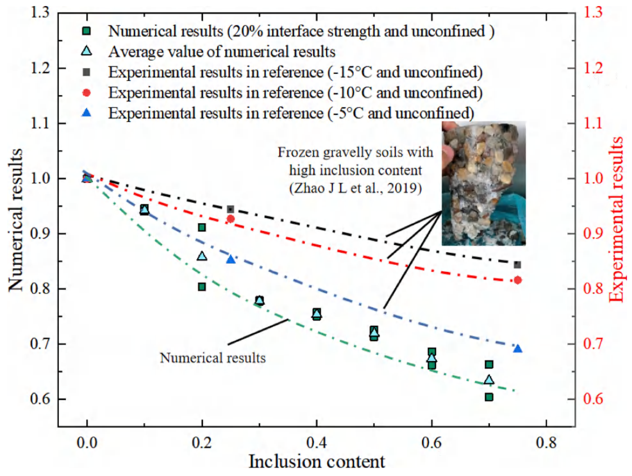

Fig. 18. Comparison of numerical and experimental results (Zhao et al., 2019).

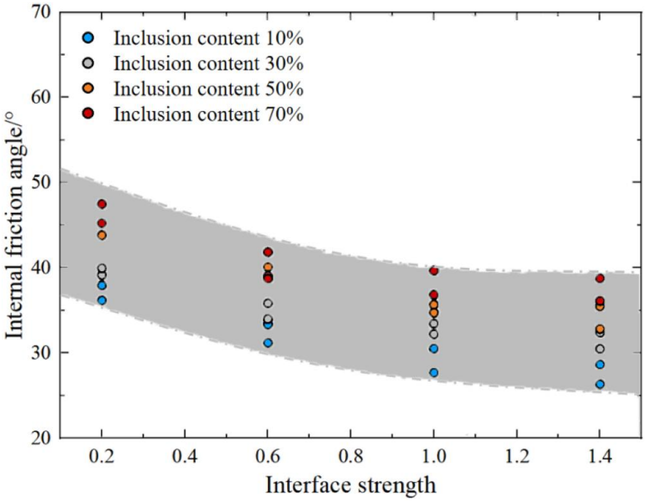

Fig. 19. Evolution of the internal friction angle with increasing interface strength.

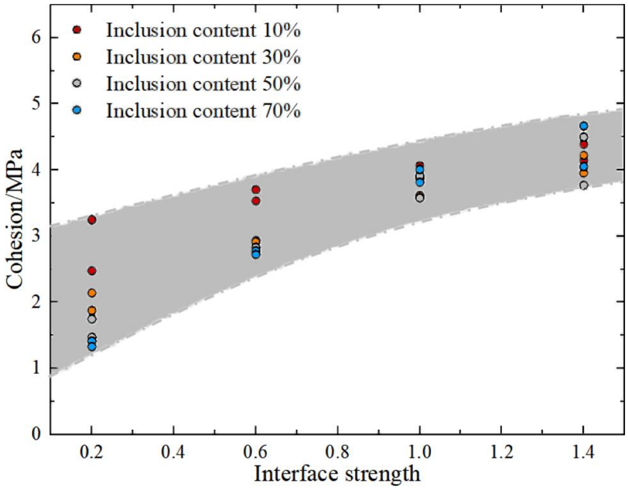

Fig. 20. Evolution of cohesion with increasing interface strength.

inclusion contents (10 %~70 %) are generated using the method proposed in Section 2. Results in Fig. 16 indicate that the effects of various spatial distributions of rock blocks are limited. Therefore, two specimens are generated for each group during sensitivity analyses considering both modeling accuracy and computational costs. Cylindrical specimens for numerical compression tests are prepared with a height of 100 mm and a diameter of 50 mm. The mechanical properties of each component are from relevant research that considered interface effects and a cemented matrix [20]. The details of the mechanical parameters are presented in Table 2. Triaxial compression tests are conducted on the fabricated specimens with various confining pressures from 0 MPa to 1 MPa. Cohesive elements are integrated into the matrix, inclusions, and interfaces to record the fracturing behaviours for each component.

4.1. Effects of interface strength on mechanical behaviour

(1) Effects on mechanical strength

For each interface strength and confining pressure, the evolution characteristic of compression strength versus inclusion content is depicted in Fig. 17. An unusual evolution trend of compression strength is observed when the interface is rather weak, i.e., 20 % of the matrix strength. As shown in Fig. 17(a), the compression strength shows a notable decrease with increasing inclusion content when the confining pressure is less than 0.5 MPa. When the confining pressure is increased to 1 MPa, the descending trend of the compression strength reverses when the inclusion content exceeds 40 %. This indicates that the increase in hard inclusions does not always benefit the mechanical properties of heterogeneous geomaterials. When the bounded states between the inclusions and matrix are quite weak, an increase in inclusions introduces a considerable number of weak interfaces. In this case, increasing weak interfaces offer many potential fracture paths during compression, which leads to less compression strength. The same behaviour is also found in the

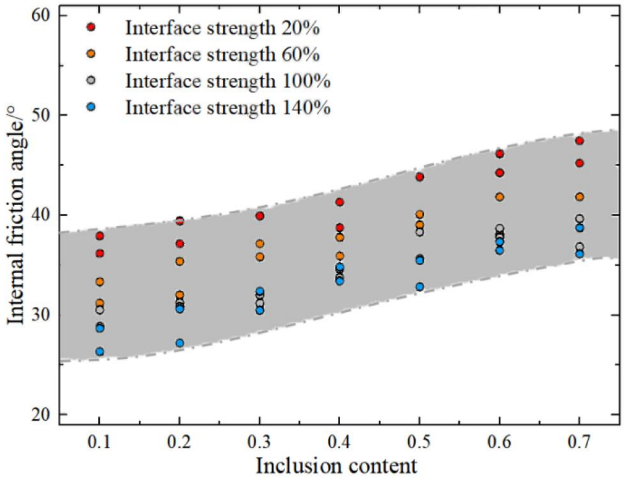

Fig. 21. Evolution of the internal friction angle with increasing inclusion content.

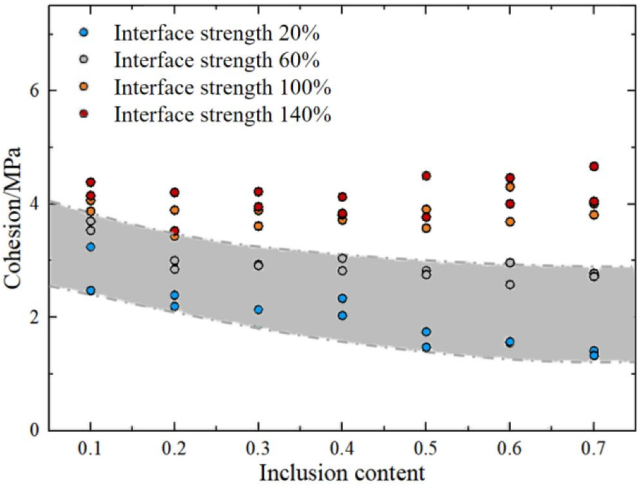

Fig. 22. Evolution of cohesion with increasing inclusion content.

experimental research on frozen gravelly soils conducted by Zhao et al. (2019). As the interface between gravel and frozen soils is composed of thin and smooth ice layers, the interface strength is much less than that of both frozen soils and gravelly inclusions. A comparison of the numerical results and the experimental results (Zhao et al., 2019) is presented in Fig. 18. Similar evolution trends prove the rationality of the numerical results. However, with increasing confining pressure and inclusion content, the positive effects of hard inclusions become pronounced again despite poorly bonded interfaces, which improves mechanical strength.

When the interface strength reaches 60 % of the matrix strength, the uniaxial compression strength fluctuates with increasing inclusion content, whereas the triaxial compression strength shows increasing trends with increasing inclusion content. It is inferred that increasing the interface strength can notably help in taking advantage of the mechanical strength of hard inclusions. With further increases in the interface strength, consistent and notable increasing trends are observed with increasing inclusion content, which is consistent with the conclusions and findings in most available studies [63,31]. The compression strength grows much more slowly when the inclusion content exceeds 50 %. It is inferred that there are interlocking effects among irregular inclusions when the inclusion content reaches 50 %, the mechanical enhancements by hard inclusions are apparent in these cases.

(2) Effects of interface strength on cohesion and internal friction angle

The cohesion and friction angle are considered fundamental parameters that govern the shear behaviours of geomaterials. The influences of the inclusion content on the shear behaviours of heterogeneous geomaterials have been investigated extensively in previous research. However, the effects of interface strength were not considered in the available studies. Based on the proposed numerical model, the effects of interface strength on shear parameters are further investigated. The results are illustrated in Fig. 19 and Fig. 20. A notable decreasing trend of the internal frictional angle is observed with increasing interface strength. It is inferred that increasing the confining pressure effectively improves the mechanical strength of heterogeneous geomaterials when the interface is

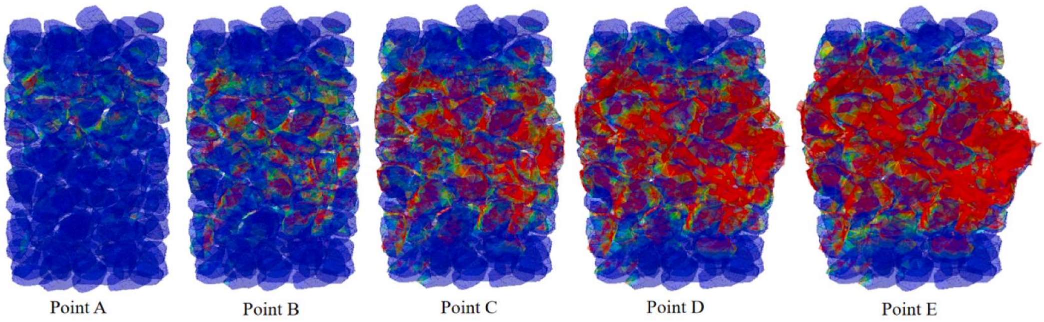

(a) Fractures at interfaces

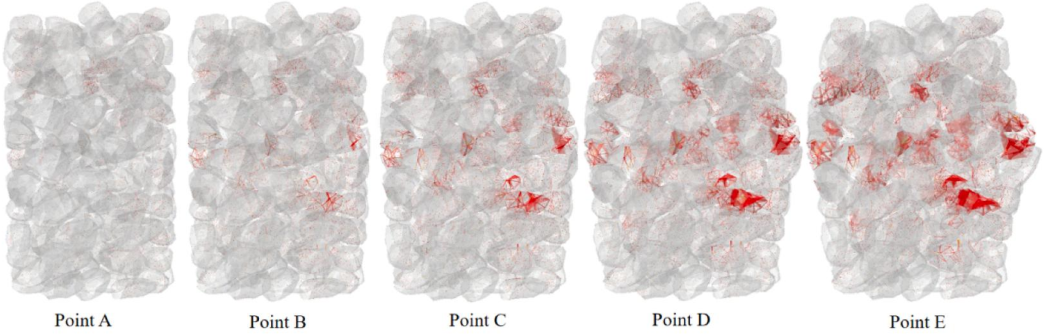

(c) Fractures in inclusions

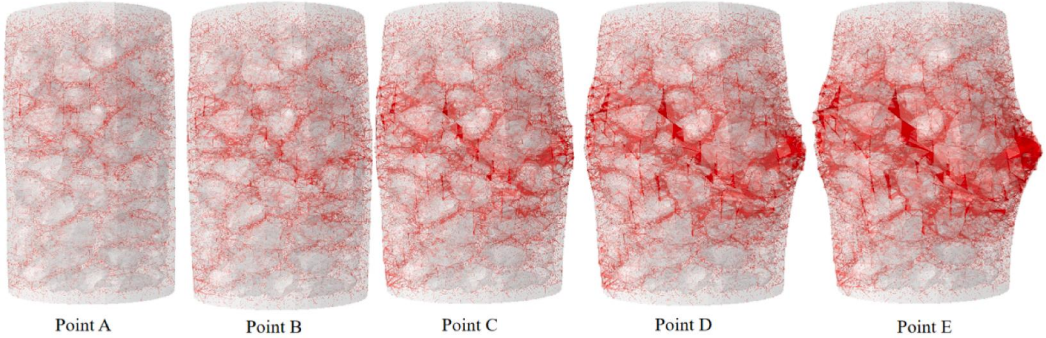

(c) Fractures in the matrix

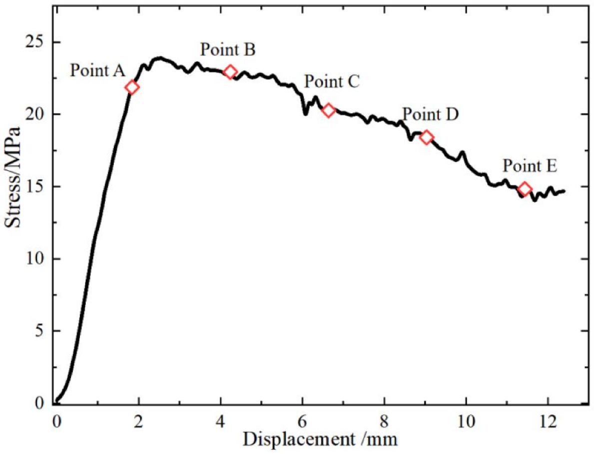

(d) Stress–displacement curve and monitoring points

(caption on next page)

Fig. 23. Evolution of fracturing.

relatively vulnerable. Regarding cohesion, consistent increasing trends are observed as the interface strength increases.

Fig. 21 and Fig. 22 show the development of cohesion and internal frictional angle as the inclusion content increases. For each interface strength, a similar and consistent growth trend of the internal friction angle is observed. It is inferred that a larger content of hard inclusions corresponds to greater sensitivity to confining pressure. However, the evolution of cohesion differs at different interface strengths. When the interface strength is less than 60 % of that of the matrix, cohesion decays notably with increasing

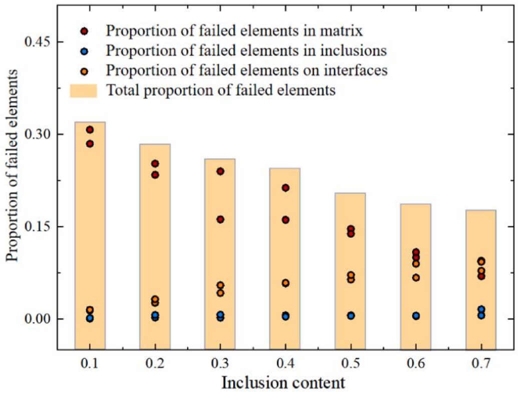

(a) Interface strength 20% and confining pressure 0 MPa

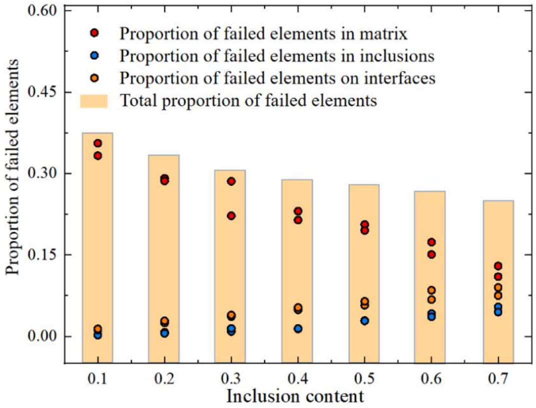

(b) Interface strength 20% and confining pressure 1 MPa

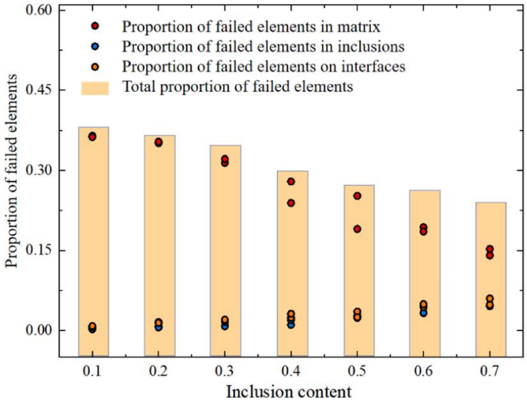

(c) Interface strength 140% and confining pressure 0 MPa

Fig. 24. Evolution of failure proportions versus inclusion contents at various interface strengths and confining pressures.

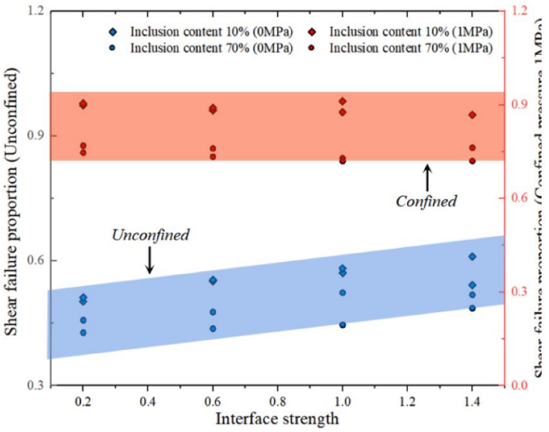

(a) Shearing failure proportion versus interface strength

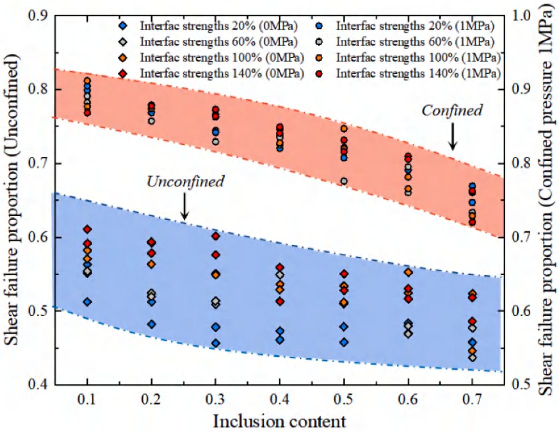

(b) Shear failure proportion versus inclusion content

Fig. 25. Evolution of shear failure proportions versus inclusion content at various interface strengths and confining pressures.

inclusion content, especially for the cases with the least interface strength. This confirms that hard inclusions do not inevitably benefit the mechanical strength of heterogeneous geomaterials. Nevertheless, when the interface strength reaches that of the matrix, no clear trend is observed between cohesion and the inclusion content.

4.2. Effects of interface strength on fracturing behaviour

Cohesive elements are inserted and used to trace and record every minor fracture of numerical specimens during the compressive process, as shown in Fig. 23. The fracturing behaviour of each component of the specimen with an inclusion content of 50 % and a confining pressure of 1 MPa are presented in Fig. 23. Comparing the fracture patterns in Fig. 23 (a) and Fig. 23 (c) shows that fractures become intensive in the regions near the interface. Multiple shearing paths are found in the matrix, and they propagate forward along the hard inclusions. Obvious dilatation behaviour is observed due to the blocking effects of hard inclusions. Fractures are also present in the hard inclusions owing to the high confining pressure.

To further investigate and understand the micromechanical behaviours of heterogeneous geomaterials, the numbers and proportions of failed cohesive elements in the matrix, inclusions, and interfaces are counted, as illustrated in Fig. 24. Statistics show that most failures occur in the matrix and at interfaces. The total proportion of failed elements decreases with increasing inclusion content in general since the proportion of the matrix component decreases significantly. However, the proportions of failed elements in different components (i.e., matrix, inclusions, and interfaces) among the total number of failed elements change obviously with different interface strengths.

When the interface strength is only 20 % of the matrix strength, the proportion of failures at the interfaces increases significantly with increasing inclusion content. According to the statistics in Fig. 24, almost all interface elements fail under this condition due to their low mechanical strength, whereas failure is rare in inclusions. Fig. 24 (a) shows that the failure of elements at interfaces accounts for over 50 % of the total number of failed elements when the inclusion content exceeds 50 %. In these situations, increasing the

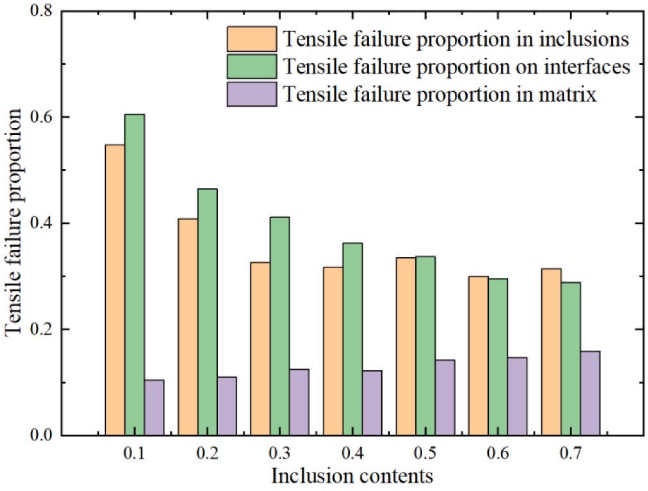

(a) Tensile failure proportion versus inclusion contents on average

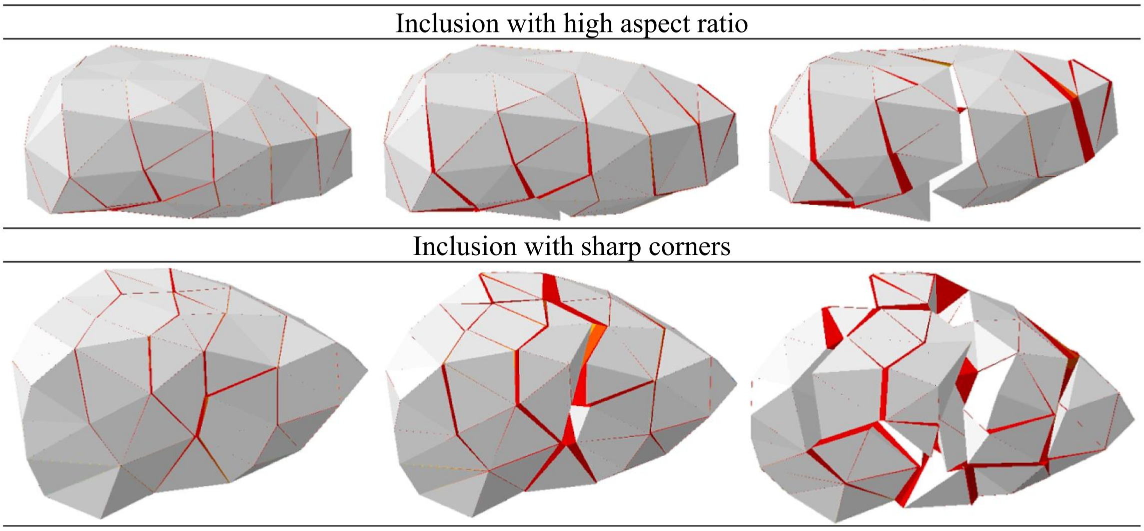

(b) Fracture characteristics

Fig. 26. Inclusion fracture characteristics.

number of weak interfaces offers multiple potential fracture paths and dominates the mechanical and fracturing behaviours of heterogeneous geomaterials, which leads to less compression strength. However, when the confining pressure is raised to 1 MPa, the proportion of failures of cohesive elements in inclusions increases notably (as shown in Fig. 24 (a)), especially when the inclusion content exceeds 50 %, which consequently improves the compression strength. These changes in the failure proportions in different components explain the internal mechanism of the reversal in the trends of the compression strength in Fig. 18(a).

A comparison of the failure proportions in Fig. 24 (a) and Fig. 24 (c) suggests that the total proportion of failed elements, the proportion of failed elements in the matrix, and the proportion of failed elements in inclusions increase obviously with increasing interface strength, whereas the proportion of failed element on interfaces decreases. It is inferred that increasing the interface strength helps to transfer external forces from the matrix to the inclusions. The increase in the proportion of failed elements in inclusions indicates that hard inclusions share a considerable part of the external forces, which contributes to the improvement in the mechanical strength of heterogeneous geomaterials. It is also noticed that the rate of decrease of the total proportion of failed elements is much more gradual with increasing inclusion content in Fig. 24 (b) and (c) compared with that in Fig. 24 (a). Thus, increasing the interface strength can cause discrete inclusions in the matrix to bear higher compression stress more effectively.

To further understand the mechanism that changes the mechanical properties of heterogeneous geomaterials, the failed cohesive elements that are mainly caused by shearing (i.e., fracture model II) are counted. The criterion that determines the failure type of a cohesive element is as follows:

Table A1
The main program used to define the established constitutive relationship.

Materials properties	$k_n, k_{s1}, k_{s2}, \sigma_n^o, \tau_{s1}^o, \tau_{s2}^o, G_I, G_{II}, G_{III}, \eta$
Variables at time t	$\{u\}^t = STATEV(1:3); D^t = STATEV(4); \{\sigma\}^t = STATEV(5:7)$
Computational values of critical parameters at time t	$\beta = \frac{\sqrt{(u_2^t)^2 + (u_3^t)^2}}{\sqrt{(u_2^t)^2 + (u_3^t)^2} + u_1^t}; B = \frac{\beta^2}{1 + 2\beta^2 - 2\beta}; G_{shear}^0 = G_{II} + G_{III}; \{u\}^t = \{u\}^t + du$ $\delta_n^o = \sigma_n^o / k_n; \delta_{s1}^o = \tau_{s1}^o / k_{s1}; \delta_{s2}^o = \tau_{s2}^o / k_{s2}; \tau_{shear}^0 = \sqrt{(\tau_{s1}^o)^2 + (\tau_{s2}^o)^2}$
Definition of the shearing type	Compression shearing ($\sigma_n^t < 0$);Tensile shearing ($\sigma_n^t > 0$);
Compression shearing ($\sigma_n^t < 0$)	$\delta_{mix}^o = \sqrt{(\delta_{s1}^o)^2 + (\delta_{s2}^o)^2};\ \tau_{shear}^{mix} = \tau_{shear}^0 + \lvert\sigma_n\rvert \times tan(\phi) k_{mix} = \tau_{shear}^{mix} / \delta_{mix}^o;\ G_{mix} = \frac{(\tau_{shear}^0 + \sigma_n \times \tan(\phi)) G_{shear}^0}{\tau_{shear}^0};\ \delta_{mix}^f = \frac{2G_{mix}}{k_{mix} \times \delta_{mix}^o}$
Tensile shearing ($\sigma_n^t > 0$)	$\delta_{mix}^o = \sqrt{(\delta_n^o)^2 + \left[(\delta_{s1}^o)^2 + (\delta_{s2}^o)^2 - (\delta_n^o)^2\right] B^\eta};$ $k_{mix} = k_n(1 - B) + k_s B;\ G_{mix} = G_I + (G_{shear}^0 - G_I) \times B^\eta;\ \delta_{mix}^f = \frac{2G_{mix}}{k_{mix} \times \delta_{mix}^o}$
Equivalent displacement	$\delta = \sqrt{(u_2^t)^2 + (u_3^t)^2}\ \sigma_n^t < 0$ $\delta = \sqrt{(u_1^t)^2 + (u_2^t)^2 + (u_3^t)^2}\ \sigma_n^t > 0$
Damage updating	$\delta^t = \frac{\delta_{mix}^o \delta_{mix}^f}{\delta_{mix}^f - D^t(\delta_{mix}^f - \delta_{mix}^o)};\ \delta^{t+1} = Max(\delta, \delta^t) D^{t+1} = \begin{cases} Min\left(1, \frac{\delta_{mix}^f(\delta^{t+1} - \delta_{mix}^o)}{\delta^{t+1}(\delta_{mix}^f - \delta_{mix}^o)}\right) & \delta > \delta^t \\ D^t & \delta \leqslant \delta^t \end{cases}$
Stress and state variables updating	$\begin{Bmatrix} \sigma_n \\ \sigma_{s1} \\ \sigma_{s2} \end{Bmatrix}^{t+1} = \begin{bmatrix} k_n(1 - D^{t+1})\ 0\ 0 \\ 0\ k_{s1}(1 - D^{t+1})\ 0 \\ 0\ 0\ k_{s2}(1 - D^{t+1}) \end{bmatrix} \begin{Bmatrix} u_1^{t+1} \\ u_2^{t+1} \\ u_3^{t+1} \end{Bmatrix} \sigma_n > 0$ $STATEV(1:3) = \{u\}^{t+1}; STATEV(4) = D^{t+1};$ $\begin{Bmatrix} \sigma_n \\ \sigma_{s1} \\ \sigma_{s2} \end{Bmatrix}^{t+1} = \begin{bmatrix} k_n\ 0\ 0 \\ 0\ k_{mix}(1 - D^{t+1})\ 0 \\ 0\ 0\ k_{mix}(1 - D^{t+1}) \end{bmatrix} \begin{Bmatrix} u_1^{t+1} \\ u_2^{t+1} \\ u_3^{t+1} \end{Bmatrix} \sigma_n < 0$ $STATEV(5:7) = \{\sigma\}^{t+1}$

Notes: The STATEV is an array containing the solution-dependent state variables.

$$D_{me} = 1 - \frac{G_n}{G_n + G_s} \tag{17}$$

where D_{me} represents the mode mix ratio during damage evolution, which varies from 0 to 1. The failure of a cohesive element is defined as a shear failure when D_{me} is greater than 0.5; otherwise, it is considered a tensile failure.

The ratio of the number of element that undergoes shear failure to the total number of failed elements is presented in Fig. 25. As shown in Fig. 25 (a), shear failure is a prevalent failure mode for each test group. Notably, increasing the interface strength and confining pressure improves the proportion of shear failure. However, a consistently decreasing trend of the shear proportion is found as the inclusion content increases for both the confined and unconfined groups, as shown in Fig. 25(b). According to the statistics of the tensile failure proportion in Fig. 26, the decreasing shearing failure proportion may be caused by the increasing tensile failure proportion in the matrix. Notably, tensile failure consists of over 30 % of the total failure in the inclusions and interfaces, as shown in Fig. 26(a). This indicates that tensile failure is also an important constituent of the failure mode in inclusions and interfaces. In addition, typical fracture patterns of irregular inclusions are presented in Fig. 26(b). Both large aspect ratios and sharp corners cause the tensile failure of inclusions during the compression process with high confining pressure. Thus, the tensile strength of hard inclusions is also a crucial parameter in determining the mechanical strengths of heterogeneous geomaterials.

5. Conclusions

A FDEM-based numerical method is developed to simulate the mechanical and fracturing behaviours of heterogeneous geomaterials with irregular inclusions. A computational geometry method, CWSVM, is developed to control the mesh quantity and quality of the raw inclusion morphology obtained from 3D scanning techniques. On this basis, the signed-distance-field-based discrete element method (SDF-DEM) is employed to model the natural spatial distribution of inclusions and large contents of inclusions. For the modelling of the fracturing process, a finite-discrete element model is developed by integrating cohesive elements into the mesh. In addition, a combined constitutive model is proposed to consider the shear-hardening behaviour of the cohesive elements. Then, the proposed numerical approach is verified through comparison with experimental results including shape characteristics and mechanical behaviour. Finally, the effects of interface strength on mechanical and fracturing behaviours are systematically investigated using the validated method. The following conclusions are drawn:

The proposed CWSVM-based surface reconstruction approach can effectively refine the inclusion geometry while retaining the main shape characteristics. Both mesh quantity and quality can be well controlled by the CWSVM. The SDF-DEM-based inclusion allocation algorithm is capable of generating stochastic numerical models effectively and efficiently, especially for cases with large fractions of inclusions.

The proposed FDEM model is validated by comparing the simulated mechanical and fracturing behaviours of inclusion-containing materials with experimental results. The numerical results agree well with the experimental results for the cases with various inclusion contents. Satisfactory calculation accuracy is achieved using the proposed FDEM model with much less computational time and lower cost than other methods.

The interface is a critical component that determines the mechanical properties of heterogeneous geomaterials. When the interfaces between the inclusions and the matrix are appropriately bonded, the mechanical properties are generally improved with increasing content of inclusions. However, the opposite trends are observed when the interface strength is less than 60 % of the matrix strength. In addition, cohesion and internal friction show opposite development trends as the interface strength increases.

Increasing the interface strength significantly improves the proportion of failures in hard inclusions, especially in cases of high confining pressures and inclusion fractions. In addition, a considerable proportion of failures at inclusions and interfaces are caused by tensile stress, which indicates that the tensile strength of hard inclusions is a critical parameter that determines the mechanical properties of inclusion-containing materials.

CRediT authorship contribution statement

Yuexiang Lin: Writing – original draft, Methodology, Conceptualization. **Jianjun Ma:** Writing – review & editing, , Formal analysis. **Zhengshou Lai:** Data curation, Modeling, Methodology. **Linchong Huang:** Writing – review & editing, Project administration. **Mingfeng Lei:** .

Declaration of Competing Interest

The authors declare that they have no known competing financial interests or personal relationships that could have appeared to influence the work reported in this paper.

Data availability

Data will be made available on request.

Acknowledgments

This work is supported by the National Natural Science Foundation of China (No. 52208381, 52278422, 51978677), and the Foundation Research Project of China (Grant: JCKY2020110C096), Science and Technology Program of Guangzhou, China (No. 202102020617). These financial supports are gratefully acknowledged.

A.Appendix.

See Table A1

References

[1] Belytschko T, Black T., Elastic crack growth in finite elements with minimal remeshing. Int J Numer Meth Eng , 1999, 45:601–620 https://doi.org/10.1002/(SICI)1097-0207(19990620)45:5<601::AID-NME598>3.0.CO;2-S.

[2] Benzeggagh ML. Measurement of mixed-mode delamination fracture toughness of unidirectional glass/epoxy composites with mixed-mode bending apparatus. Composites Science and Technology 1996;56(04):439–49. https://doi.org/10.1016/0266-3538(96)00005-x.

[3] Du X, Zhang P, Jin L, Lu D. A multi-scale analysis method for the simulation of tunnel excavation in sandy cobble stratum. Tunnel Under S Tech 2018;83: 220–30. https://doi.org/10.1016/j.tust.2018.09.019.

[4] Fang C, Gong J, Jia M, Nie Z, Li B, Ashiru M, et al. DEM simulation of the shear behaviour of breakable granular materials with various angularities. Adv Powder Technol 2021;32(11):4058–69. https://doi.org/10.1016/j.apt.2021.09.009.

[5] Guo J, Luo B, Lu C, Lai J, Ren J. Numerical investigation of hydraulic fracture propagation in a layered reservoir using the cohesive zone method. Eng Fract Mech 2017;186:195–207. https://doi.org/10.1016/j.engfracmech.2017.10.013.

[6] Gong J, Liu J, Cui L. Shear behaviors of granular mixtures of gravel-shaped coarse and spherical fine particles investigated via discrete element method. Powder Technol 2019;353(15):178–94. https://doi.org/10.1016/j.powtec.2019.05.016.

[7] Gong J, Wang X, Liang L, et al. DEM study of the effect of fines content on the small-strain stiffness of gap-graded soils 2019;112:35–40. https://doi.org/10.1016/j.compgeo.2019.04.008.

[8] Gong J, Zou J, Zhao L, Li L, Nie Z. New insights into the effect of interparticle friction on the critical state friction angle of granular materials. Comput Geotech 2019;113:103105. https://doi.org/10.1016/j.compgeo.2019.103105.

[9] Huang G, Xu Y, Yi X, Xia M. An Efficient Disk-Based Discontinuous Deformation Analys is Model for Simulating Large-Scale Problems. Int j geo 2020;20(7). https://doi.org/10.1061/(ASCE)GM.1943-5622.0001711.

[10] Huang G, Zhang S, Xu Y. A sphere-triangle contact model with complex boundary face problems. Appl Math Model 2020;93:395–411. https://doi.org/10.1016/j.apm.2020.12.030.

[11] Huang G, Tong C, Zhang S, Chen X. A thermo-solid coupling model for disk discontinuous deformation analysis to simulate heating and stirring particles in rotary drums. Powder Technol 2022;402:117326. https://doi.org/10.1016/j.powtec.2022.117326.

[12] Lai Z, Chen Q. Reconstructing granular particles from X-ray computed tomography using the TWS machine learning tool and the level set method. Acta Geotech 2019;14:1–18. https://doi.org/10.1007/s11440-018-0759-x.

[13] Lai Z, Huang L. A polybézier-based particle model for the DEM modeling of granular media. Comput Geotec 2021;134:104052. https://doi.org/10.1016/j.compgeo.2021.104052.

[14] Lai Z, Zhao S, Zhao J, Huang L. Signed distance field framework for unified DEM modeling of granular media with arbitrary particle shapes. Comput Mech 2022;70:763–83. https://doi.org/10.1007/s00466-022-02220-8.

[15] Li M, Guo P, Stolle D, Liang L. Development of hydraulic fracture zone in heterogeneous material based on smeared crack method. J Nat Gas Sci Engng 2016;35:761–74. https://doi.org/10.1016/j.jngse.2016.09.018.

[16] Li M, Guo P, Stolle D, Liang L. Modeling method for a rock matrix with inclusions distributed and hydraulic fracturing characteristics. J Petrol Sci Eng 2017;157:409–21. https://doi.org/10.1016/j.petrol.2017.07.017.

[17] Li M, Guo P, Stolle D, Liang L, Shi Y. Modeling hydraulic fracture in heterogeneous rock materials using permeability-based hydraulic fracture model. Poro mechanicsV 2020;5(2):167–83. https://doi.org/10.1016/j.undsp.2018.12.005.

[18] Li M, Guo P, Stolle D, Liu S, Liang L. Heterogeneous rock modeling method and characteristics of multistage hydraulic fracturing based on the PHF-LSM method. J Nat Gas Sci Engng 2020;83:103518. https://doi.org/10.1016/j.jngse.2020.103518.

[19] Li M, Guo P, Stolle D, Sun S, Liang L. Modeling hydraulic fracture propagation in a saturated porous rock media based on EPHF method. J Nat Gas Sci Eng 2021;89:103887. https://doi.org/10.1016/j.jngse.2021.103887.

[20] Lin Y, Yin Z, Wang X, Huang L. A systematic 3D simulation method for geomaterials with block inclusions from image recognition to fracturing modelling. Theor Appl Fract Mech 2021;117:103194. https://doi.org/10.1016/j.tafmec.2021.103194.

[21] Lin Y, Wang X, Ma J, Huang L. A systematic framework for the 3D finite-discrete modelling of binary mixtures considering irregular block shapes and cohesive block-matrix interfaces. Powder Technol 2021;117070. https://doi.org/10.1016/j.powtec.2021.117070.

[22] Lin Y, Wang X, Ma J, Huang L. A finite-discrete element based appoach for modelling the hydraulic fracturing of rocks with irregular inclusions. Eng Fract Mech 2022;108209. https://doi.org/10.1016/j.engfracmech.2021.108209.

[23] Lin Y, Li C, Ma J, Lei M. Effects of void morphology on fracturing characteristics of porous rock through a finite-discrete element method. J Nat Gas Sci Eng 2022;104684. https://doi.org/10.1016/j.jngse.2022.104684.

[24] Ma J, Chen J, Guan J, Lin Y, Chen W, Huang L. Implementation of Johnson-Holmquist-Beissel model in four-dimensional lattice spring model and its application in projectile penetration. Int J Impact Eng 2022;170:104340. https://doi.org/10.1016/j.ijimpeng.2022.104340.

[25] Nie Z, Fang C, Gong J, Liang Z. DEM study on the effect of roundness on the shear behaviour of granular materials. Comput Geotech 2018;121:103457. https://doi.org/10.1016/j.compgeo.2020.103457.

[26] Nie Z, Liang Z, Wang X. A three-dimensional particle roundness evaluation method. Granul Matter 2020;20(2):32. https://doi.org/10.1007/s10035-018-0802-5.

[27] Qu T, Di S, Feng Y, Wang M, Zhao T. Towards data-driven constitutive modelling for granular materials via micromechanics-informed deep learning. Int J Plast 2021;144:103046. https://doi.org/10.1016/j.ijplas.2021.103046.

[28] Qu T, Wang M, Feng Y. Applicability of discrete element method with spherical and clumped particles for constitutive study of granular materials. Jour Rock Mech Geo Eng 2021;14(1):240–51. https://doi.org/10.1016/j.jrmge.2021.09.015.

[29] Sun L, Liu Q, Grasselli G, Tang X. Simulation of thermal cracking in anisotropic shale formations using the combined finite-discrete element method. Comput Geotech 2020;117:103237. https://doi.org/10.1016/j.compgeo.2019.103237.

[30] Turon A, Camanho PP, Costa J, Dávilac CG. A damage model for the simulation of delamination in advanced composites under variable-mode loading. Mech Mater 2006;38(11):1072–89. https://doi.org/10.1016/j.mechmat.2005.10.003.

[31] Wang H, Cui Y, Lamas-Lopez F, Dupla J, Canou J, Calon N, et al. Effects of inclusion contents on resilient modulus and damping ratio of unsaturated track-bed materials. Can Geo J 2017;54(12):1672–81. https://doi.org/10.1139/cgj-2016-0673.

[32] Wang H, Cui Y, Lamas-Lopez F, Dupla J, Canou J, Calon N, et al. Permanent deformation of track-bed materials at various inclusion contents under large number of loading cycles. Geotech Geoenviron Eng 2018;144(8):04018044. https://doi.org/10.1061/(ASCE)GT.1943-5606.0001911.

[33] Wang H, Cui Y, Lamas-Lopez F, Calon N, Saussine G, Dupla J, et al. Investigation on the mechanical behavior of track-bed materials at various contents of coarse grains. Constr Build Mater 2018;164:228–37. https://doi.org/10.1016/j.conbuildmat.2017.12.209.

[34] Wang P, Yin Z, Wang Z. Micromechanical Investigation of Particle-Size Effect of Granular Materials in Biaxial Test with the Role of Particle Breakage. J Eng Mech 2021;148(1):04021133. https://doi.org/10.1061/(ASCE)EM.1943-7889.0002039.

[35] Wang P, Yin Z, Zhou W, Chen W. Micro-mechanical analysis of soil–structure interface behavior under constant normal stiffness condition with DEM. Acta Geotech 2021. https://doi.org/10.1007/s11440-021-01374-8.

[36] Wang X, Nie Z, Gong J, Liang Z. Random generation of convex aggregates for DEM study of particle shape effect. Constr Build an Mater 2021;268:121468. https://doi.org/10.1016/j.conbuildmat.2020.121468.

[37] Wang Y, Li X, Wu YF, Lin C, Zhang B. Experimental study on meso-damage cracking characteristics of RSA by CT test. Environ Earth Sci 2015;73(9):5545–58. https://doi.org/10.1007/s12665-014-3808-2.

[38] Wang Y, Li X, Zheng B, He JM, Li SD. Macro–meso failure mechanism of soil–rock mixture at medium strain rates. Géo Lett 2016;6(1):28–33. https://doi.org/10.1680/jgele.15.00118.

[39] Wang Y, Li CH, Hu YZ. Use of x-ray computed tomography to investigate the effect of rock blocks on meso-structural changes in soil-rock mixture under triaxial deformation. Constr Build Mater 2018;164:386–99. https://doi.org/10.1016/j.conbuildmat.2017.12.173.

[40] Wang Y, Li CH, Hu YZ. 3D image visualization of meso-structural changes in a bimsoil under uniaxial compression using x-ray computed tomography (CT). Eng Geo 2019;248:61–9. https://doi.org/10.1016/j.enggeo.2018.11.004.

[41] Wei D, Wang J, Nie J, Zhou B. Generation of realistic sand particles with fractal nature using an improved spherical harmonic analysis. Comput Geotech 2018;104:1–12. https://doi.org/10.1016/j.compgeo.2018.08.002.

[42] Wu Z, Xu X, Liu Q, Yang Y. A zero-thickness cohesive element-based numerical manifold method for rock mechanical behavior with micro-Voronoi grains. Eng Anal Bound Elem 2018;96:94–108. https://doi.org/10.1016/j.enganabound.2018.08.005.

[43] Wang T, Yan C, Wang G, Zheng Y, Ke W, Jiao Y. Numerical study on the deformation and failure of soft rock roadway induced by humidity diffusion. Tunn Undergr Space Technol 2022;126:104565. https://doi.org/10.1016/j.tust.2022.104565.

[44] Wang S, Li D, Hani M, Li H. Numerical simulation of hydraulic fracture deflection influenced by slotted directional boreholes using XFEM with a modified rock fracture energy model - ScienceDirect. J Petrol Sci Engng 2020;193:107375. https://doi.org/10.1016/j.petrol.2020.107375.

[45] Wang S, Li D, Li Z, Liu J, Gong S, Li G. A rate-dependent model and its user subroutine for cohesive element method to investigate propagation and branching behavior of dynamic brittle crack 2021;136:104233. https://doi.org/10.1016/j.compgeo.2021.104233.

[46] Wang S, Li Z, Yuan R, Li G, Li D. A shear hardening model for cohesive element method and its application in modeling shear hydraulic fractures in fractured reservoirs 2020;83:103580. https://doi.org/10.1016/j.jngse.2020.103580.

[47] Yan C, Zheng H, Sun G, Ge X. Combined finite-discrete element method for simulation of hydraulic fracturing. Rock Mech Rock Eng 2016;49(4):1389–410. https://doi.org/10.1007/s00603-015-0816-9.

[48] Yan C, Zheng H. A coupled thermo-mechanical model based on the combined finite-discrete element method for simulating thermal cracking of rock. Int J Rock Mech Min Sci 2017;91:170–8. https://doi.org/10.1016/j.ijrmms.2016.11.023.

[49] Yan C, Jiao Y, Zheng H. A fully coupled three-dimensional hydro-mechanical finite discrete element approach with real porous seepage for simulating 3D hydraulic fracturing. Comput Geotech 2018;96:73–89. https://doi.org/10.1016/j.compgeo.2017.10.008.
[50] Yan C, Jiao Y, Zheng H. A three-dimensional heat transfer and thermal cracking model considering the effect of cracks on heat transfer. Int J Numer Anal Methods Geomech 2019;43(2). https://doi.org/10.1002/nag.2937.
[51] Yan C, Zheng H, Huang D, Wang G. A coupled contact heat transfer and thermal cracking model for discontinuous and granular media. Comput Methods Appl Mech Eng 2021;375:113587. https://doi.org/10.1016/j.cma.2020.113587.
[52] Yan C, Wang T, Ke W, Wang G. A 2D FDEM-based moisture diffusion-fracture coupling model for simulating soil desiccation cracking. Acta Geotech 2021;16: 2609–28. https://doi.org/10.1007/s11440-021-01297-4.
[53] Yan C, Xie X, Ren Y, Ke W, Wang G. A FDEM-based 2D coupled thermal-hydro-mechanical model for multiphysical simulation of rock fracturing. Int J Rock Mech Min Sci 2022;149:104964. https://doi.org/10.1016/j.ijrmms.2021.104964.
[54] Yan C, Wei D, Wang G. Three-dimensional finite discrete element-based contact heat transfer model considering thermal cracking in continuous-discontinuous media. Comput Methods Appl Mech Engng 2022;388:114228. https://doi.org/10.1016/j.cma.2021.114228.
[55] Yan C, Guo H, Tang Z. Three-dimensional continuous-discrete pore-fracture mixed seepage model and hydromechanical coupling model to simulate rock fracture driven by fluid. J Petrol Sci Engng 2022;215(B):110510. https://doi.org/10.1016/j.petrol.2022.110510.
[56] Yang Kuijian, Liyu Rao, Hu Lingling, et al. Flexible, efficient and adaptive modular impact-resistant metamaterials. International Journal of Mechanical Sciences 2023;239:107893. https://doi.org/10.1016/j.ijmecsci.2022.107893.
[57] Yang Kuijian, Li Zekai. Quasi-static and dynamic out-of-plane crashworthiness of 3D curved-walled mixed-phase honeycombs. Thin-Walled Structures 2023; 182:110305. https://doi.org/10.1016/j.tws.2022.110305.
[58] Yin P, Zhao G. Stochastic reconstruction of Gosford sandstone from surface image. Int J Rock Mech Min Sci 2014;70:82–9. https://doi.org/10.1016/j.ijrmms.2014.04.012.
[59] Yin P, Ma J, Yan C, Huang L. Estimation of the shear strength of fractured Gosford sandstone based on fractal theory and numerical modelling. Journal of Petroleum Science and Engineering 2019;182:106278. https://doi.org/10.1016/j.petrol.2019.106278.
[60] Yin ZY, Wang P, Zhang FS. Effect of particle shape on the progressive failure of shield tunnel face in granular soils by coupled FDM-DEM method. Tunnel Space Tech 2020;100:103394. https://doi.org/10.1016/j.tust.2020.103394.
[61] Zhai L, Zhang H, Pan D, Zhu Y, Zhu J, Zhang Y, et al. Optimisation of hydraulic fracturing parameters based on cohesive zone method in oil shale reservoir with random distribution of weak planes. J Nat Gas Sci Eng 2020;75:103130. https://doi.org/10.1016/j.jngse.2019.103130.
[62] Zhang HY, Xu WJ, Yu YZ. Triaxial tests of soil–rock mixtures with different rock block distributions. Poro mechanicsV 2016;56(1):44–56. https://doi.org/10.1016/j.sandf.2016.01.004.
[63] Zhang P, Lu D, Du X, Qi J. A division method for shallow tunnels and deep tunnels considering soil stress path dependency. Comput Geo 2021;1351:104012. https://doi.org/10.1016/j.compgeo.2021.104012.
[64] Zhang P, Du X, Lu D, Liu J, Qi J. Study on the excavation disturbed zone during tunneling in sandy cobble stratum considering the material meso-structure. Trans Geo 2021;29:100590. https://doi.org/10.1016/j.trgeo.2021.100590.
[65] Zhang P, Jin L, Du X, Lu D. Computational homogenization for mechanical properties of sand cobble stratum based on fractal theory. Eng Geo 2018;232(8): 82–93. https://doi.org/10.1016/j.enggeo.2017.11.013.
[66] Zhang ZL, Xu WJ, Xia W, Zhang HY. Large-scale in-situ test for mechanical characterization of soil–rock mixture used in an embankment dam. Int J Rock Mech Min 2016;86:317–22. https://doi.org/10.1016/j.ijrmms.2015.04.001.
[67] Zhao LH, Huang DL, Zhang Shuaihao, et al. A new method for constructing finite difference model of soil-rock mixture slope and its stability analysis. International Journal of Rock Mechanics and Mining Sciences 2021;138:104605. https://doi.org/10.1016/j.ijrmms.2020.104605.
[68] Zhou B, Wang J, Wang H. A novel particle tracking method for granular sands based on spherical harmonic rotational invariants. Géo 2018;68(12):1116–23. https://doi.org/10.1680/jgeot.17.T.040.
[69] Zhou B, Wang J, Wang H. Three-dimensional sphericity, roundness and fractal dimension of sand particles. Géo 2017;68(1):18–30. https://doi.org/10.1680/jgeot.16.P.207.